



Parallel Application of Slitless Spectroscopy to Analyze Galaxy Evolution (PASSAGE): Survey Overview

Matthew A. Malkan¹ , Vihang Mehta² , Ayan Acharyya³ , Hollis B. Akins⁴ , Anahita Alavi² , Hakim Atek⁵ , Ivano Baronchelli⁶ , Andrew J. Battisti^{7,8,9} , Kit Boyett^{9,10,11} , Marusa Bradac¹² , Sean Tyler Bruton¹³ , Andrew J. Bunker¹¹ , Adam J. Burgasser¹⁴ , Caitlin M. Casey^{4,15,16} , Nuo Chen¹⁷ , James Colbert² , Y. Sophia Dai¹⁸ , Maximilien Franco^{4,19} , Clea Hannahs¹ , Santosh Harish²⁰ , Farhanul Hasan²¹ , Matthew J. Hayes²² , Alaina L. Henry²¹ , Mason Huberty¹³ , Tucker Jones²³ , Jeyhan S. Kartaltepe²⁰ , Keunho J. Kim² , Nicha Leethochawalit²⁴ , Jacob Levine¹ , Sijia Li^{25,26} , Yu-Heng Lin² , Yixiao Liu¹⁸ , Charlotte Mason²⁷ , Daniel Masters²⁸ , Henry Joy McCracken²⁹ , Takahiro Morishita² , Kalina V. Nedkova^{21,28} , Marc Rafelski^{21,28} , Vivasvaan Aditya Raj¹ , Guido Roberts-Borsani³⁰ , Axel Runnholm²² , Michael J. Rutkowski³¹ , Alberto Saldana-Lopez^{21,28} , Zahra Sattari² , Claudia Scarlata¹³ , Kasper Borello Schmidt¹ , Marko Shuntov^{16,33} , Harry Teplitz³⁴ , Michele Trenti^{9,10} , Tommaso Treu¹ , Benedetta Vulcani³ , Peter J. Watson³ , Xin Wang^{18,25,35} , and Zhuyun Zhuang³⁴

¹ University of California, Los Angeles, Department of Physics and Astronomy, 430 Portola Plaza, Los Angeles, CA 90095, USA; malkan@astro.ucla.edu

² IPAC, California Institute of Technology, 1200 E. California Blvd, Pasadena, CA 91125, USA

³ INAF, Osservatorio Astronomico di Padova, Vicolo dell'Osservatorio 5, 35122 Padova, Italy

⁴ The University of Texas at Austin, 2515 Speedway Blvd Stop C1400, Austin, TX 78712, USA

⁵ CNRS, Institut d'Astrophysique de Paris, 98 bis Boulevard Arago, 75014 Paris, France

⁶ INAF, Istituto di Radioastronomia, Via Piero Gobetti 101, 40129 Bologna, Italy

⁷ International Centre for Radio Astronomy Research (ICRAR), University of Western Australia, M468, 35 Stirling Highway, Crawley, WA 6009, Australia

⁸ Australian National University, Research School of Astronomy and Astrophysics, Canberra, ACT 2611, Australia

⁹ ARC Centre of Excellence for All Sky Astrophysics in 3 Dimensions (ASTRO 3D), Australia

¹⁰ School of Physics, University of Melbourne, Parkville 3010, VIC, Australia

¹¹ University of Oxford, Department of Physics, Keble Road, Oxford OX1 3RH, UK

¹² University of Ljubljana, Department of Physics, Jadranska ulica 19, 1000 Ljubljana, Slovenia

¹³ University of Minnesota, Twin Cities, 116 Church St SE, Minneapolis, MN 55455, USA

¹⁴ University of California, San Diego, Center for Astrophysics and Space Sciences, 9500 Gilman Drive, La Jolla, CA 92093, USA

¹⁵ Department of Physics, University of California, Santa Barbara, Santa Barbara, CA 93106, USA

¹⁶ Cosmic Dawn Center (DAWN), Denmark

¹⁷ The University of Tokyo, Graduate School of Science, Department of Astronomy, 7-3-1 Hongo, Bunkyo-ku, Tokyo 113-0033, Japan

¹⁸ Chinese Academy of Sciences South America Center for Astronomy (CASSACA), National Astronomical Observatories (NAOC), 20A Datun Road, Beijing 100012, People's Republic of China

¹⁹ Université Paris-Saclay, Université Paris Cité, CEA, CNRS, AIM, 91191 Gif-sur-Yvette, France

²⁰ Laboratory for Multiwavelength Astrophysics, School of Physics and Astronomy, Rochester Institute of Technology, 84 Lomb Memorial Drive, Rochester, NY 14623, USA

²¹ Space Telescope Science Institute, 3700 San Martin Drive, Baltimore, MD 21218, USA

²² Stockholm University, Department of Astronomy, AlbaNova University Center, SE-106 91 Stockholm, Sweden

²³ Department of Physics and Astronomy, University of California, Davis, 1 Shields Avenue, Davis, CA 95616, USA

²⁴ National Astronomical Research Institute of Thailand (NARIT), Mae Rim, Chiang Mai, 50180, Thailand

²⁵ School of Astronomy and Space Science, University of Chinese Academy of Sciences (UCAS), Beijing 100049, People's Republic of China

²⁶ Department of Astronomy, Xiamen University, Xiamen, Fujian 361005, People's Republic of China

²⁷ University of Copenhagen, Niels Bohr Institute, Juliane Maries Vej 30, DK-2100 Copenhagen, Denmark

²⁸ The Johns Hopkins University, Department of Physics and Astronomy, 3400 N. Charles Street, Baltimore, MD 21218, USA

²⁹ Institut d'Astrophysique de Paris, UMR 7095, CNRS, and Sorbonne Université, 98 bis boulevard Arago, F-75014 Paris, France

³⁰ Department of Astronomy, University of Geneva, Chemin Pegasi 51, CH-1290 Versoix, Switzerland

³¹ Minnesota State University, Mankato, Department of Physics and Astronomy, 141 Trafton Science Center N, Mankato, MN 56001, USA

³² Department of Astronomy, Oskar Klein Centre, Stockholm University, 106 91 Stockholm, Sweden

³³ Niels Bohr Institute, University of Copenhagen, Jagtvej 128, DK-2200, Copenhagen, Denmark

³⁴ California Institute of Technology, 1200 E. California Blvd, Pasadena, CA 91125, USA

³⁵ Institute for Frontiers in Astronomy and Astrophysics, Beijing Normal University, Beijing 102206, People's Republic of China

Received 2024 November 22; revised 2025 August 25; accepted 2025 August 27; published 2025 October 30

Abstract

During the second half of Cycle 1 of the James Webb Space Telescope (JWST), we conducted the Parallel Application of Slitless Spectroscopy to Analyze Galaxy Evolution (PASSAGE) program. PASSAGE received the largest allocation of JWST observing time in Cycle 1, 591 hr of NIRISS observations to obtain direct near-IR imaging and slitless spectroscopy. About two-thirds of this was ultimately executed, to observe 63 high-latitude fields in pure-parallel mode. These have provided more than 10,000 near-infrared grism spectrograms of faint galaxies. PASSAGE brings unique advantages in studying galaxy evolution: (a) Unbiased spectroscopic search, without prior photometric preselection. By including the typical galaxies which have low masses and strong emission lines, slitless spectroscopy is the indispensable complement to any pretargeted spectroscopy. (b) The



Original content from this work may be used under the terms of the [Creative Commons Attribution 4.0 licence](https://creativecommons.org/licenses/by/4.0/). Any further distribution of this work must maintain attribution to the author(s) and the title of the work, journal citation and DOI.

combination of several dozen independent fields to overcome cosmic variance. (c) Near-infrared spectral coverage, spanning a wide wavelength range of up to 1.0 to 2.3 μm , with minimal wavelength gaps, to measure multiple diagnostic rest-frame optical lines, minimizing sensitivity to dust reddening. (d) JWST’s unprecedented spatial resolution, in some cases using two orthogonal grism orientations, to overcome contamination due to blending of overlapping spectra. (e) Discovery of rare bright objects especially for detailed JWST follow-up. PASSAGE data are public immediately, and our team plans to deliver fully processed high-level data products. In this PASSAGE overview, we describe the survey and data quality, and present examples of these accomplishments in several areas of current interest in the evolution of emission-line galaxy properties, particularly at low masses.

Unified Astronomy Thesaurus concepts: James Webb Space Telescope (2291); Galaxies (573); Early universe (435); Galaxy evolution (594); Emission line galaxies (459)

1. Introduction

The value of unbiased spectroscopic selections of galaxies has long been recognized for understanding their evolution across cosmic time. For emission-line galaxies, this can crudely be done with ground-based imaging through narrow-band filters (A. J. Bunker et al. 1995; H. I. Teplitz et al. 1999; N. Kashikawa et al. 2006, 2011; C. Ly et al. 2007, 2012; G. D. Becker et al. 2018). Full spectral surveys have been done using grism spectroscopy with Hubble Space Telescope (HST)/NICMOS (P. J. McCarthy et al. 1999; L. Yan et al. 1999; E. K. S. Hicks et al. 2002; B. E. Backhaus et al. 2024), and then with HST/WFC3 (H. Atek et al. 2010; A. Henry et al. 2013, 2021; M. Malkan & WISP Team 2013; T. Treu et al. 2015; M. B. Bagley et al. 2017; A. J. Battisti et al. 2024). More recently, JWST has also used grisms to obtain slitless spectroscopy of large samples of galaxies (M. Bradač et al. 2024; V. Estrada-Carpenter et al. 2024; X. He et al. 2024; G. Rihtaršič et al. 2025; P. J. Watson et al. 2025).

Cosmic star formation likely peaked at $z \sim 2-3$ (C. Ly et al. 2009; P. Madau & M. Dickinson 2014). Most of our knowledge of galaxies at these epochs is restricted to massive ones. We know less about the more representative galaxies with $\log(M_*/M_\odot) \leq 10$, as samples are sparse and biased, with the stacking of spectra with low signal-to-noise ratio (S/N) often being required (e.g., A. Henry et al. 2013, 2021; R. L. Sanders et al. 2018). Parallel NIRISS slitless spectroscopy is revolutionizing our understanding of galaxy evolution at high redshifts, especially in the important low-mass regime. By combining many fields with moderate depth, plus smaller numbers of deep fields, PASSAGE obtains coverage of statistically powerful numbers of galaxies spanning a very wide range of luminosities and stellar masses. We are measuring key optical emission-line diagnostics, including [O II] $\lambda\lambda 3726, 3729$, [O III] $\lambda\lambda 4959, 5007$, [S II] $\lambda\lambda 6716, 6724$ and hydrogen Balmer lines, across a wide range of redshift ($z = 1-3.5$), and Paschen and [S III] $\lambda\lambda 9532, 9069$ lines at lower redshifts, for of the order of 10,000 galaxies—by far the largest sample ever assembled.

In this paper we discuss our new PASSAGE observations in Section 2, the data reduction and sensitivity in Section 3, some examples of scientific results in Section 4, and future prospects in Section 5.

2. Observations

2.1. Slitless Spectroscopy with NIRISS

The Near Infrared Imager and Slitless Spectrograph (NIRISS) instrument on the James Webb Space Telescope (JWST) enables near-infrared slitless spectroscopy (0.8–2.3 μm) with two orthogonal medium-resolution ($R \sim 150$ at 1.4 μm)

grisms over a $133'' \times 133''$ field of view (C. J. Willott et al. 2022; R. Doyon et al. 2023). NIRISS employs a set of specialized broad filters (PASSAGE uses F115W, F150W, and F200W) to selectively transmit specific wavelength ranges of infrared light, crucial for isolating key spectral features while blocking out-of-band radiation. The filters work in conjunction with the NIRISS grisms (GR150R and GR150C), enabling slitless spectroscopy by dispersing light across the detector, along either rows or columns, respectively. The combination of these filters and grisms helps minimize contamination from overlapping spectral orders and maximizes sensitivity in the target wavelength range, making them essential for capturing detailed spectrograms of faint astronomical sources. By using multiple filters in sequence, NIRISS can construct a comprehensive spectral profile of objects.

For Cycle 1 of JWST, a large program of pure-parallel spectroscopy received an allocation of 591 hr. PASSAGE, JWST-1571 (PI: Malkan), began in 2022 December, when the pure-parallel observing mode first became available for scheduling. Pure-parallel observations, as implied, are executed simultaneously with a separate instrument (NIRISS in our case) in parallel while a primary instrument is being used by a different guest observer program. JWST pure-parallel observations are subject to various constraints imposed by the prime observation. A collection of prime observations were assigned to our program where we were allowed to craft an observing strategy for the NIRISS pure-parallel observations—we refer to these as parallel opportunities.

Scheduling pure-parallel slitless spectroscopy is challenging. Ideally, each wavelength setting requires three filter wheel motions (for a direct image and spectra with both orthogonal orientations of the dispersion axis). However, to eliminate any risk of losing telescope guiding, these changes can only be made when the primary observers are simultaneously reconfiguring their instrument, and not taking data. In many parallel opportunities, this restricts the number of wavelengths that can be covered, especially when the primary observer is mosaicking more than one sky region.

We individually crafted observations of each available pure-parallel field to optimize the use of every parallel opportunity, down to 1.5 hr in length. These PASSAGE observations were adapted to any combination of primary exposure times and filter changes. Since the primary objective of the PASSAGE survey was to maximize the wavelength range of the spectroscopy, in opportunities with more allowed filter changes, our first priority was to extend wavelength coverage by adding spectroscopy through more broadband blocking filters (F115W, F150W, and F200W). The secondary objective when defining the observations was to reduce contamination due to overlapping spectra, and hence our next priority was to

Table 1
Observed PASSAGE Fields with Their Target Coordinates and Exposure Times

Field	R.A. (deg)	Decl. (deg)	Obs. Date	F115W Direct (hr)	F150W Direct (hr)	F200W Direct (hr)	F115W Grism (hr)	F150W Grism (hr)	F200W Grism (hr)
Par001	170.0267050	6.5888780	2022-12-17	0.43	0.86	...	2.30*	4.60*	...
Par002	177.1453720	52.7788100	2022-12-28	0.86	0.43	...	3.45*	3.45*	...
Par003	150.4103960	2.4051780	2022-12-30	0.62	1.24*
Par004	186.7047850	21.6989890	2022-12-31	1.15	1.15
Par005	150.6536980	2.0855800	2023-01-07	0.43	0.43	...	2.29*	2.29*	...
Par006	150.6762160	2.1293050	2023-01-06	0.43	0.43	...	2.29*	2.29*	...
Par007	102.4303090	70.3818910	2023-01-08	0.89	0.89
Par008	170.1264770	6.7062310	2023-01-12	0.86	1.72*
Par009	183.1322960	27.4870880	2023-01-13	0.52	1.19*
Par010	205.5720260	9.3080670	2023-02-21	0.17	3.01	1.00	...
Par011	204.5789780	-19.8794780	2023-02-22	2.61	2.61
Par012	221.6227940	-23.2860630	2023-02-25	0.01	1.91
Par013	130.5298840	1.6983950	2023-03-19	...	0.52	...	0.67	0.52	...
Par014	224.3278890	24.7169780	2023-03-23	0.67	0.67
Par015	155.4060630	18.1657440	2023-04-08	10.52	18.04
Par016	152.6594150	-4.7508000	2023-04-14	...	0.29	0.14	1.19	0.29	0.29
Par017	150.3011090	1.8910820	2023-04-19	3.15	3.15
Par018	159.2102450	1.7162860	2023-04-20	...	0.67	...	1.10	1.10	...
Par019	130.3650700	48.6033460	2023-04-20	0.10	0.10	...	0.86	0.86	...
Par020	149.6229230	2.2251060	2023-04-23	...	0.13	...	4.87	1.05	...
Par021	161.1635170	33.9294610	2023-04-24	0.52	0.67	0.67	0.57
Par022	177.2619900	22.4367760	2023-04-28	3.15	3.15
Par023	150.0655290	2.5519210	2023-05-01	...	0.13	...	4.29	1.05	...
Par024	150.1315240	2.4996600	2023-05-02	...	0.13	...	4.87	1.05	...
Par025	150.2457730	1.9774740	2023-05-02	...	0.13	...	4.87	1.05	...
Par026	150.1227170	2.4398770	2023-05-06	...	0.13	...	4.87	1.05	...
Par027	172.9448010	-12.3606500	2023-05-09	0.29	0.29	0.29	2.58*	1.15	1.15
Par028	150.0874070	2.4185310	2023-05-20	1.79	1.43	1.43	21.26*	7.08*	5.37*
Par029	150.2522870	1.7285570	2023-05-22	...	0.13	...	4.87	1.05	...
Par030	216.0875670	24.2475070	2023-05-25	...	0.79	...	0.79	0.79	...
Par031	187.7406480	12.5610560	2023-05-31	0.41	6.49
Par032	180.4252840	-18.8087340	2023-06-07	...	1.00	...	1.00	1.00	...
Par033	176.4223950	20.3820560	2023-06-09	0.95	0.95
Par034	190.4031030	22.4995390	2023-06-21	1.24	1.24	1.24	6.20*	1.24	1.24
Par035	181.5579470	-8.6302920	2023-06-21	2.98	2.98
Par036	184.2851990	2.7440130	2023-06-21	0.20	2.03
Par037	180.3574960	2.3583210	2023-06-23	0.48	0.48	...	1.91	1.91	...
Par038	215.1343710	53.0534480	2023-06-25	...	0.13	...	4.87	4.87	...
Par039	182.9192700	-1.1318990	2023-06-29	0.67	3.82
Par040	181.3629010	-7.5363050	2023-07-01	0.95	0.95	0.95	0.95
Par041	191.4234500	3.5618430	2023-07-02	0.43	3.44
Par042	195.1846320	12.5341350	2023-07-04	...	0.57	0.57	2.58	1.00	1.00
Par043	213.2233650	-3.2187080	2023-07-25	0.14	0.14
Par044	265.7442370	67.0902050	2023-09-03	0.14	2.10	0.52	0.57
Par045	137.7250700	-4.4086120	2023-11-17	0.95	3.01
Par046	149.3468690	2.5384070	2023-12-03	0.20	1.62
Par047	149.4398780	2.1723810	2023-12-03	0.20	1.62
Par048	149.4029130	1.6714440	2023-12-03	0.20	1.62
Par049	149.7024380	2.0589470	2023-12-03	0.20	1.62
Par050	189.1800240	62.0654160	2023-12-22	...	2.04	2.04	12.02*	3.94	3.94
Par051	150.5036630	2.2633940	2024-01-02	0.79	7.09*
Par052	150.1552210	2.0418390	2024-01-03	...	2.04	1.36	12.02*	3.94	3.94
Par053	150.1030700	1.7931780	2024-01-04	0.20	1.62
Par054	214.5759310	52.2796830	2024-01-15	4.29	4.29	4.29	4.29
Par055	177.4168450	22.1796790	2024-01-16	...	0.79	...	0.79	0.79	...
Par056	169.9978930	6.5094450	2024-01-22	...	0.79	0.79	...	1.57	1.57
Par057	177.4628390	22.2952510	2024-01-24	0.67	0.91	0.91	0.67
Par058	177.5042440	22.6834370	2024-05-16	4.51	4.51	4.51	4.51
Par059	169.9723860	6.7628470	2024-05-19	...	1.43	...	2.86	1.43	...
Par060	157.5820920	5.5249110	2024-05-26	0.43	1.15
Par061	159.1929810	-2.4619510	2024-06-01	0.43	0.43	...	2.30*	2.30*	...
Par062	188.1922630	9.3749900	2024-06-20	0.20	2.23

Table 1
(Continued)

Field	R.A. (deg)	Decl. (deg)	Obs. Date	F115W Direct (hr)	F150W Direct (hr)	F200W Direct (hr)	F115W Grism (hr)	F150W Grism (hr)	F200W Grism (hr)
Par063	149.9702590	-22.8246010	2023-12-09	0.14	0.14

Note. The target coordinates represent an average field center in cases of multiple pointings per field. For times marked with an asterisk (*), the total exposure time is split between the G150R and G150C grisms.

add observations with the second GR150 grism (usually GR150C after GR150R), providing spectrograms at a second, orthogonal, orientation. We excluded potential fields at Galactic latitudes below 20° to avoid spectrum overlaps in crowded fields.

Table 1 presents the PASSAGE Observing Log, detailing the sky coordinates of all NIRISS field centers observed to date, along with the exposure times for both direct imaging and spectroscopy in each wave band. While our exposure times were constrained by the scheduling of prime observations, we consistently assigned the longer integrations to spectroscopy, ensuring that the grism exposures have equal or greater duration than the imaging. The sky locations of these observations are illustrated in Figures 1 and 2.

Because the fainter emission lines of interest ($\text{Ly}\alpha$ and $[\text{O II}]$) generally fall in the shorter-wavelength spectral coverage, in all medium- and long-exposure parallel fields, we typically integrated 2–2.5 times longer in that F115W broadband filter (1.0–1.3 μm) than in the longer-wavelength filters. Most of the shorter parallel fields (up to 4 hr total) were devoted entirely to spectroscopy through the F200W broadband filter (1.7–2.3 μm), because this long-wavelength region was inaccessible to slitless spectroscopy with WFC3 on HST (A. J. Battisti et al. 2024). The detailed breakdown of exposure combinations for the survey is illustrated in the pie chart of Figure 3. Four out of the 63 PASSAGE fields have multiple combinations of orientations and filters, leading to a double counting in the wheel of Figure 3. For instance, a field that was observed with F115W at two position angles (PAs), and with F150W and F200W at only 1 PA, contributes to both the purple and orange slices. Therefore, the numbers of fields in the wheel sum up to 67, rather than 63.

2.2. Emission-line Detection Sensitivity

In the fields covered by pure-parallel visits longer than 3 hr, we usually obtained minimum total integration times of 4800 s in two grism filters. The main difference in the longer opportunities was the addition of longer integrations in the F115W filter (by factors of 2–3 times). Therefore our sensitivity in the F150W and F200W filters, as shown for some examples in Figure 4, was fairly uniform over most of our planned observations: for point sources, the line sensitivity was typically around $(3\text{--}4) \times 10^{-18} \text{ erg s}^{-1} \text{ cm}^{-2}$ (5σ). This limiting line flux for $\text{H}\alpha$ is equivalent to a star formation rate (SFR) $\sim 0.5 M_\odot \text{ yr}^{-1}$ at $z \sim 2$ for a Chabrier initial mass function (R. C. Kennicutt 1998). Throughout, this paper assumes a flat ΛCDM cosmology with $H_0 = 70 \text{ km s}^{-1} \text{ Mpc}^{-1}$ and $\Omega = 0.3$.

We confirm the predictions of the exposure time calculator³⁶; for a spatially extended galaxy (a Sérsic profile with major and minor axes of 1.0×0.5), the limiting emission-line flux in the central four pixels (a 0.13×0.13 box) was three times higher.

These estimates are independently confirmed by published grism spectroscopy in a NIRISS field (K. Boyett et al. 2022). Although their integrations were somewhat shorter than what we typically obtained, the line flux sensitivities are consistent with our predictions, allowing detections of one or more rest-frame optical emission lines in more than 90% of their targeted galaxies.

In the shallow fields, we devoted the more limited time to the reddest grism (F200W), since its 1.8–2.3 μm coverage has never been available for any slitless spectroscopy prior to JWST (J. Colbert et al. 2024). The emphasis was on line pairs close in wavelength, viewed at higher redshifts: $\text{H}\beta + [\text{O III}]$ and $\text{H}\alpha + [\text{S II}] \lambda\lambda 6716, 6731$.

Contrary to a widely held perception, confusion due to spectral overlap is not generally very serious during the assembly of this sample of NIRISS slitless spectra. This is because the actual spectra of all objects in a typical high-latitude field cover only a small fraction of the detector area. The low spectral resolution results in spectra that are usually confined to only $6 \times 60 = 360$ pixels, which is only 1/10,000 of the total Teledyne H2RG detector area. Therefore, in most PASSAGE observations, only $\leq 15\%$ of the spectrograms suffer from serious overlap with a spectrum of another object. The second-order spectrograms are longer but about 100 times fainter than the first-order spectrograms. Thus, the only second-order spectra that cause significant contamination tend to be from bright Galactic stars, which is noted in our output files. Since we avoided fields at low Galactic latitude, this contamination is very minor.

3. Data Reduction

Reduction of grism data is an important challenge not only for JWST, but also other ongoing and future missions (Euclid, Roman; M. B. Bagley et al. 2020; Euclid Collaboration et al. 2023). Getting the most out of NIRISS/WFSS observations requires extensive, careful data reduction efforts. For the preliminary reduction of our data, we use the Grism Redshift & Line analysis (GRIZLI;³⁷ G. Brammer 2023) software, which is a quantitative and comprehensive modeling and fitting tool for slitless spectroscopic observations. The details of our reduction will be fully described in a future publication, but we include a brief description here.

³⁶ <https://jwst-docs.stsci.edu>

³⁷ <https://grizli.readthedocs.io> version 1.9.5.

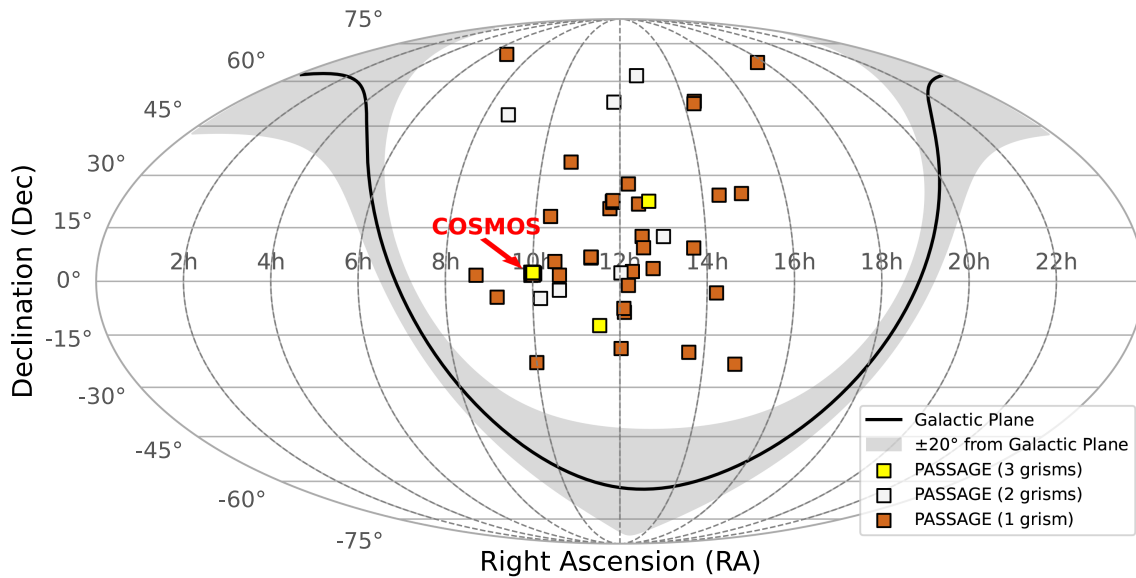


Figure 1. Sky locations of the final observed 63 PASSAGE fields, shown in Equatorial coordinates. Note that some fields overlap on the scale of this diagram. In particular, the 18 PASSAGE fields in the COSMOS field all overlap in a single yellow box in this low-resolution sky map. These are resolved in the zoom-in of the COSMOS region shown in Figure 2.

GRIZLI incorporates the default STScI data reduction pipeline to apply the initial detector-level corrections (performed by `Detector1` stage of the STScI pipeline³⁸), which includes a variety of steps such as linearity correction, persistence correction, flat-fielding, masking of bad pixels and cosmic rays, dark subtraction, and ramp fitting. GRIZLI further incorporates a custom algorithm for “snowball” masking³⁹ (`snowblind`; J. Davies 2024). This is followed by GRIZLI’s preprocessing step, which registers the World Coordinate System, performs astrometric alignment, subtracts sky background, and drizzles each exposure on a common reference frame to provide fully reduced individual exposures as well as mosaics for both the direct and dispersed images. All of our images are aligned to the Legacy Survey’s DR9 (A. Dey et al. 2019) astrometry. The next step is to identify all sources by running “Source Extraction and Photometry” (`SEP`⁴⁰; E. Bertin & S. Arnouts 1996; K. Barbary 2016) on a detection image typically created by combining all filters where a direct image is available. The absolute flux calibration is performed on individual spectra using the calibration files provided as part of the NGDEEP calibration (S. Ravindranath & Niriss Team 2023; N. Pirzkal et al. 2024).

In order to model the overlapping spectrograms, which present one of the most challenging aspects of slitless spectroscopy, GRIZLI uses the segmented images of all detected sources (brighter than m_{AB} ranging from 26 to 30, chosen depending on the depth of the direct imaging of the field), and models their associated spectrograms in each individual grism exposure. The pixels associated with an overlapping (contaminating) source are downweighted when modeling spectral energy distributions (SEDs) of the primary source of interest and extracting the final grism spectra. Lastly, GRIZLI generates the 2D dispersed spectra by simultaneously modeling each grism exposure, allowing for independent noise and other features such as differences in morphological

broadening per exposure. The final 1D spectra generated for each individual object are then modeled using a set of SED templates from EAZY⁴¹ to assist in redshift identification.

The zeroth-order contamination is of prime concern since it can masquerade as an emission line, as discussed below. The second order is only prominent for bright stars and is therefore relatively rare. When modeling the contamination, GRIZLI flags contributions from both the zeroth and second orders, and these pixels are appropriately excluded when fitting the galaxy spectra.

For the brightest objects we measure, the systematic uncertainty in the flux scales becomes a significant additional source of error. Judging from the agreement of independent but overlapping spectra of the same object, our absolute fluxes may sometimes be systematically uncertain by up to 15%. The fluxing uncertainty is worse at the blue and red edges of each spectrum. GRIZLI does not accurately correct the fluxes where the grism transmission drops below 50%. In these small edge regions, we do not attempt to measure emission-line fluxes because they are not trustworthy. Therefore we restrict our flux measurements to these reliably fluxed spectral windows: F115W: 1.013–1.283 μm , F150W: 1.330–1.671 μm , and F200W: 1.751–2.240 μm (see also Figure 4 and the graphical illustrations of the spectral windows in the one-dimensional plots of Figures 5–10). We warn other users of NIRISS that grism spectroscopy fluxes beyond these wavelength regions should not be used.

Experience with NIRISS grism spectra reduced by the GRIZLI software package showed that it picks up a significant number of artifacts (e.g., emission lines from other nearby sources, diffraction spikes, other image artifacts, modeling issues with the continuum, overlapping spectra or zeroth orders, etc.). These were incorrectly identified as real sources, which must be removed by (our) human intervention. Another problem is that when spectra of two objects partially overlap, GRIZLI’s attempt to automatically remove the contamination often leads to oversubtraction. This usually causes parts of the

³⁸ <https://jwst-pipeline.readthedocs.io>

³⁹ <https://github.com/mpj-astronomy/snowblind>

⁴⁰ <https://sep.readthedocs.io>

⁴¹ <https://eazy-py.readthedocs.io>

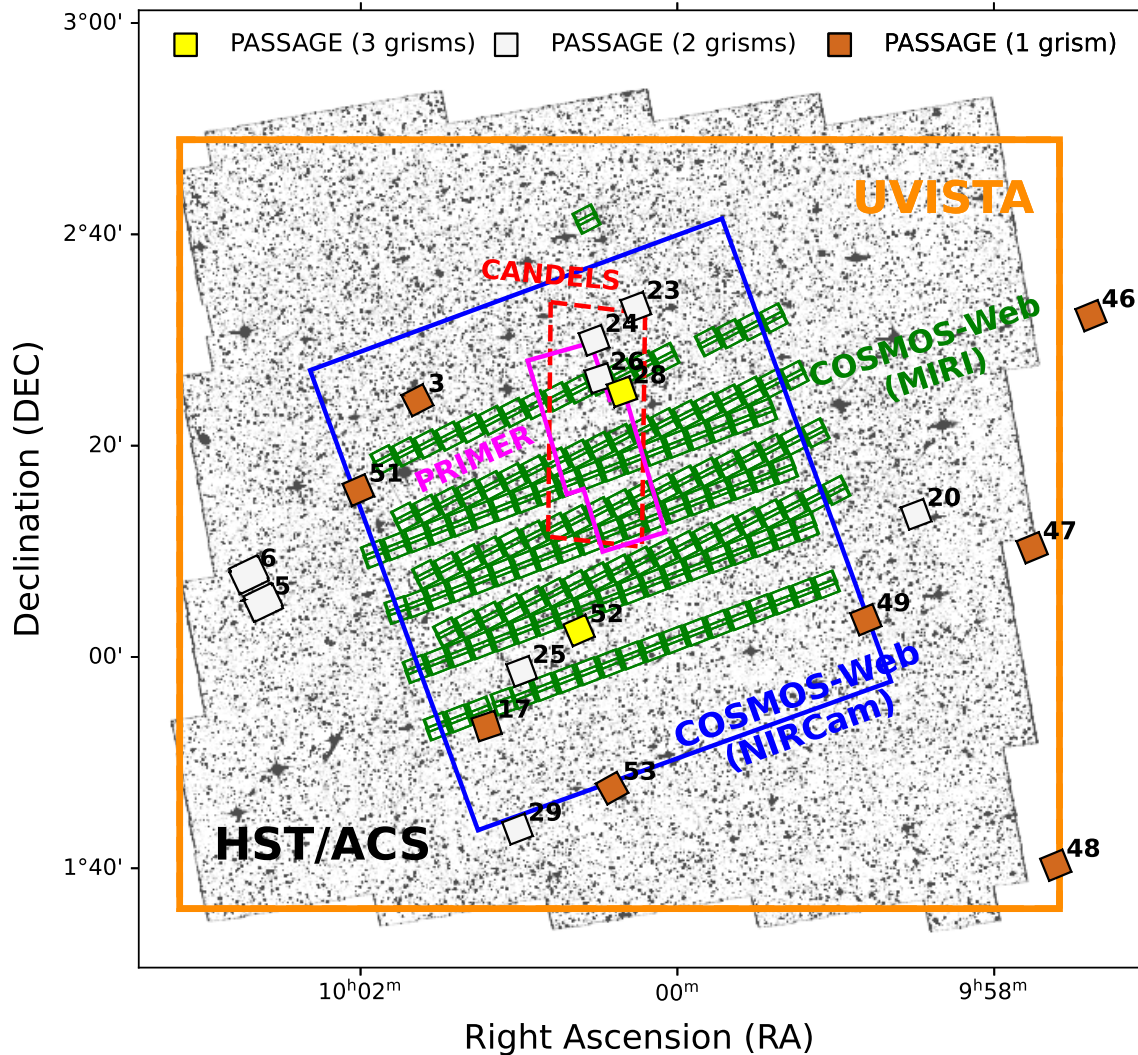


Figure 2. Zoom-in on PASSAGE fields located in and around the COSMOS field. The background is the Hubble ACS mosaic of the COSMOS field (A. M. Koekemoer et al. 2007; N. Scoville et al. 2007), along with the deep CANDELS survey as a red outline (N. A. Grogin et al. 2011; A. M. Koekemoer et al. 2011). The orange outline shows the UltraVISTA imaging survey footprint of the COSMOS field (H. J. McCracken et al. 2012). The blue and green outlines are the COSMOS-Web NIRCam and MIRI coverage, respectively (C. M. Casey et al. 2023). The magenta outline is the coverage of the PRIMER JWST survey (GO #1837).

overlapping spectra to (artificially) drop below zero flux. Efforts to replace some of this labor-intensive work with computer algorithms are ongoing.

4. PASSAGE Science Examples with Faint Emission-line Galaxies

The resulting PASSAGE spectra are of great value for investigating many questions of strong current interest in research on galaxy evolution. Our predicted number of emission-line-determined redshifts for the entire PASSAGE survey is shown in Figure 11. We now provide a few examples of relevant emission-line galaxy properties at intermediate redshifts that we are measuring with PASSAGE data.

4.1. Star Formation Main Sequence

According to equilibrium growth models (S. J. Lilly et al. 2013; L. J. Tacconi et al. 2020), galaxy evolution is controlled by cosmic accretion, merging, galactic gas depletion and star formation, and gas recycling into the circumgalactic medium.

Models of these mechanisms aim to reproduce the observed scaling relations between galaxy stellar mass, SFR, metallicity, gas content, size, and structure (e.g., K. G. Noeske et al. 2007; A. Saintonge et al. 2011; A. van der Wel et al. 2014; R. Maiolino & F. Mannucci 2019; K. V. Nedkova et al. 2021), along with their evolution over cosmic time. Observed relations appear to show large scatter, whose origin is debated. This can be modeled by short-term stochasticity, long-term differences in growth histories or gas fractions, or different scenarios for feedback from active galactic nuclei and star formation (S. J. Lilly et al. 2013; X. Ma et al. 2016; R. Davé et al. 2017, 2019; M. E. De Rossi et al. 2017; P. Torrey et al. 2018, 2019). At low masses, it is unknown whether these relations change or break down completely (H. Atek et al. 2014; A. Alavi et al. 2016; R. Amorín et al. 2017).

Unlike massive galaxies, low-mass ones often have high specific SFRs (normalized by stellar mass), with extremely strong high-ionization emission lines, elevated ionizing power, and perhaps low dust content. To test and constrain the stochastic star formation histories of hydrodynamical

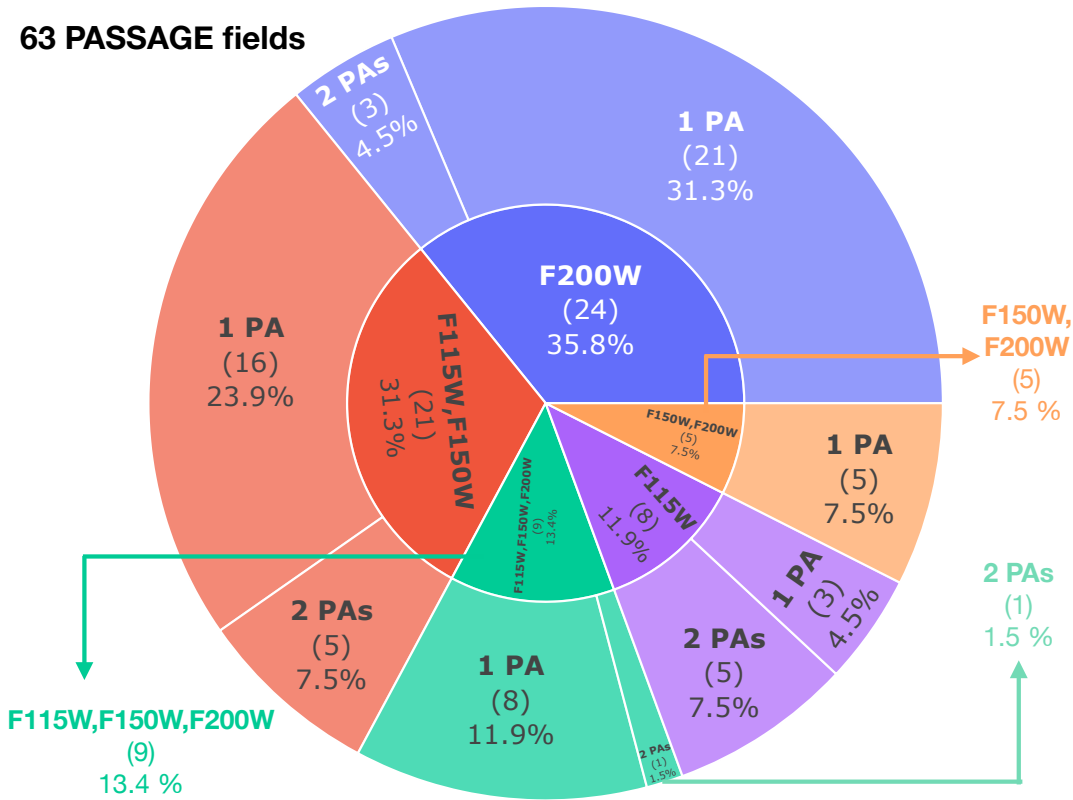


Figure 3. Pie chart showing the distribution of overlap percentages across different JWST filters (F115W, F150W, F200W) used in PASSAGE. The inner ring divides the observations into spectra with one, two, and three filters. The outer rings further separate these observations into those observed with a single grism (“1 PA,” signifying that the spectra are dispersed at a single position angle) and those observed with both the GR150R and GR150C grisms. The total numbers of fields in each category are given in parentheses. The total numbers in the wheel sum up to 67, rather than 63, due to the four fields, such as Par027, that were observed with two different combinations of filters and orientations.

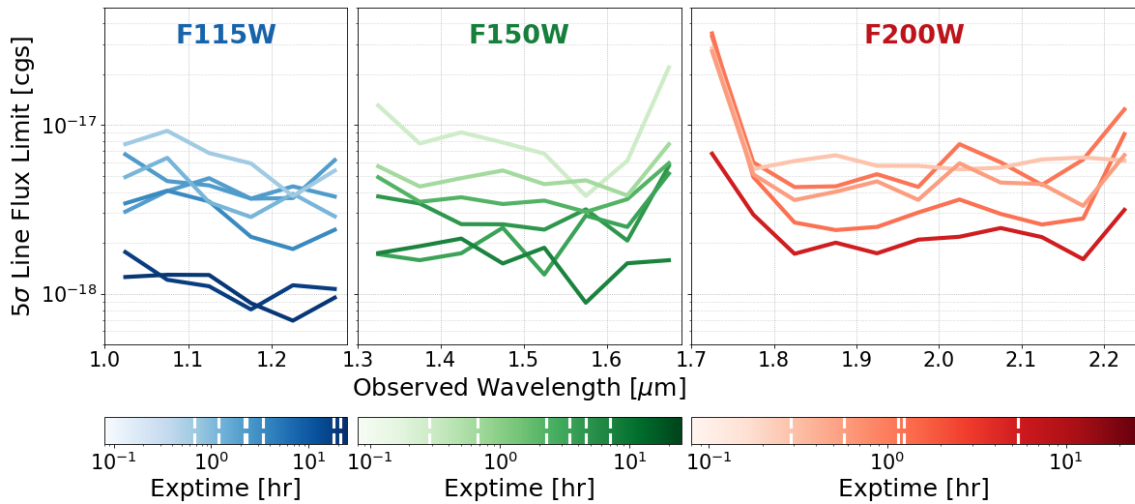


Figure 4. Emission-line flux sensitivity in typical PASSAGE observations. The 5σ detection limits, in $\text{erg s}^{-1} \text{cm}^{-2}$ are shown for point sources in several representative fields, with integration times ranging from our shortest to our longest exposures.

simulations (S. Shen et al. 2014; A. Domínguez et al. 2015; M. Sparre et al. 2017; K. Boyett et al. 2024), we are deriving SFRs from the Balmer emission lines, which reflect the star formation activity on a timescale of a few Myr. The SFR is derived from the $H\alpha$ emission line, following the calibration of R. C. Kennicutt & N. J. Evans (2012). Where available, the Balmer line ratios (e.g., $H\alpha/H\beta$) allow us to estimate the effects of dust reddening. In our representative medium field,

we measured the Balmer decrement in a sample of 122 galaxies. We derived a median value of $E(B - V)$ of 0.01 or 0.02, using the J. A. Cardelli et al. (1989) attenuation law or the SMC extinction law (K. D. Gordon et al. 2003), respectively.

Figure 12 presents the star formation main sequence (SFMS) of galaxies at $z \sim 1-2$ in a representative medium-depth field. Stellar masses were estimated via SED fitting,

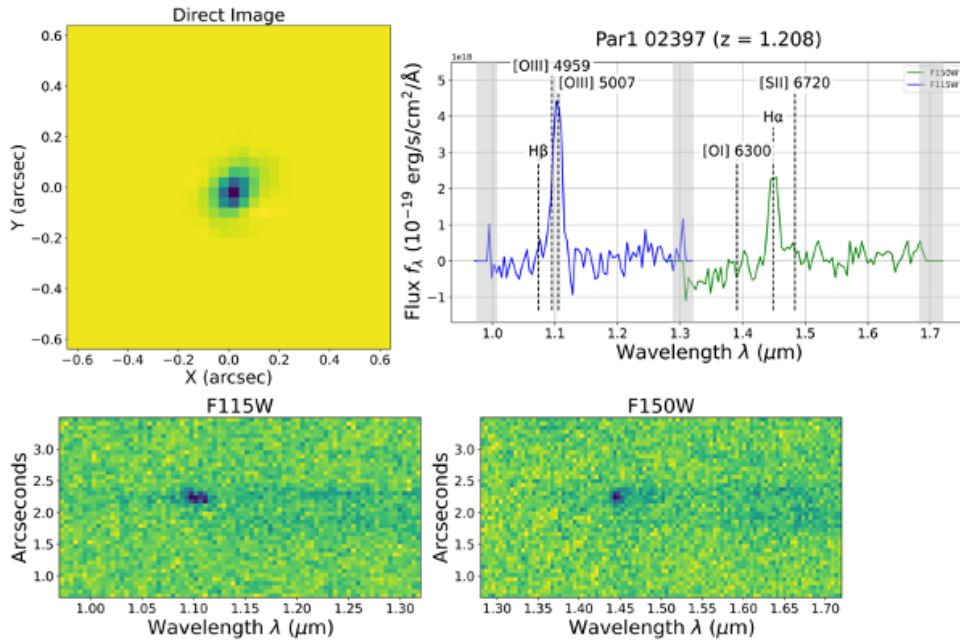


Figure 5. Example of an extreme emission-line galaxy from the Par 1 field. The upper left panel shows the broadband direct image, $1''.28$ on a side (32×32 pixels at $0''.04 \text{ pixel}^{-1}$), drizzled with `grizli` and oriented with north up. The lower rectangular panel shows the two-dimensional spectrogram at the native $0''.066 \text{ pixel}^{-1}$ scale, and the upper right displays the extracted one-dimensional spectrum. The flux scale is unreliable near the blue/red ends of each filter, shown by the full vertical gray rectangles.

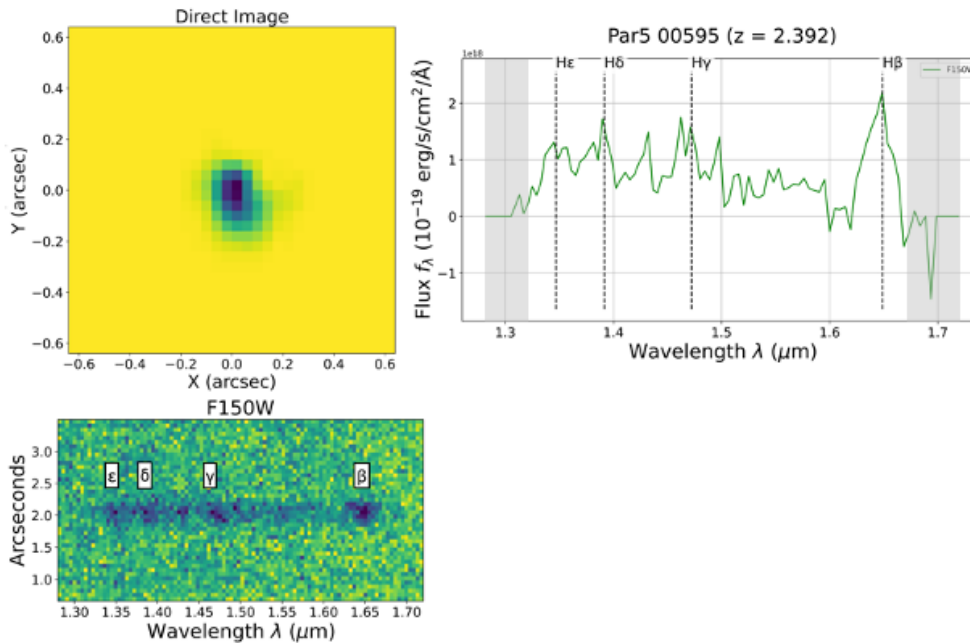


Figure 6. Another example of an extreme emission-line galaxy, displayed in the same layout as Figure 5. This compact galaxy from the Par 5 field shows a prominent Balmer series with emission visible up to He.

using a combination of our PASSAGE broadband photometry and COSMOS-Web imaging, which covers this field (see Section 4.2). Out of the 63 PASSAGE fields, 18 have overlapping coverage with COSMOS-Web (Figure 2).

Photometric fluxes were obtained within $1''$ apertures across the following bands: HST/Advanced Camera for Surveys (ACS) F814W; JWST/NIRISS F115W, F150W, F200W; JWST/NIRCam F115W, F150W, F277W, F444W; and JWST/MIRI F770W. We used the BAGPIPES software (A. C. Carnall et al. 2018) to perform the SED fitting. We

adopted a nonparametric star formation history using the continuity prior of J. Leja et al. (2019), with five logarithmically spaced age bins (fixing the most recent to cover 0–30 Myr). The metallicity was allowed to vary between 0.01 and $2.5 Z_{\odot}$, and the logarithm of the ionization parameter between -3.5 and -2 . Nebular emission was included for populations as old as 20 Myr, and dust attenuation was parameterized following J. A. Cardelli et al. (1989), with $R_V = 3.1$, and A_V varying between zero and two magnitudes. Star formation rates, $\text{SFR}_{\text{H}\alpha}$, were computed using the

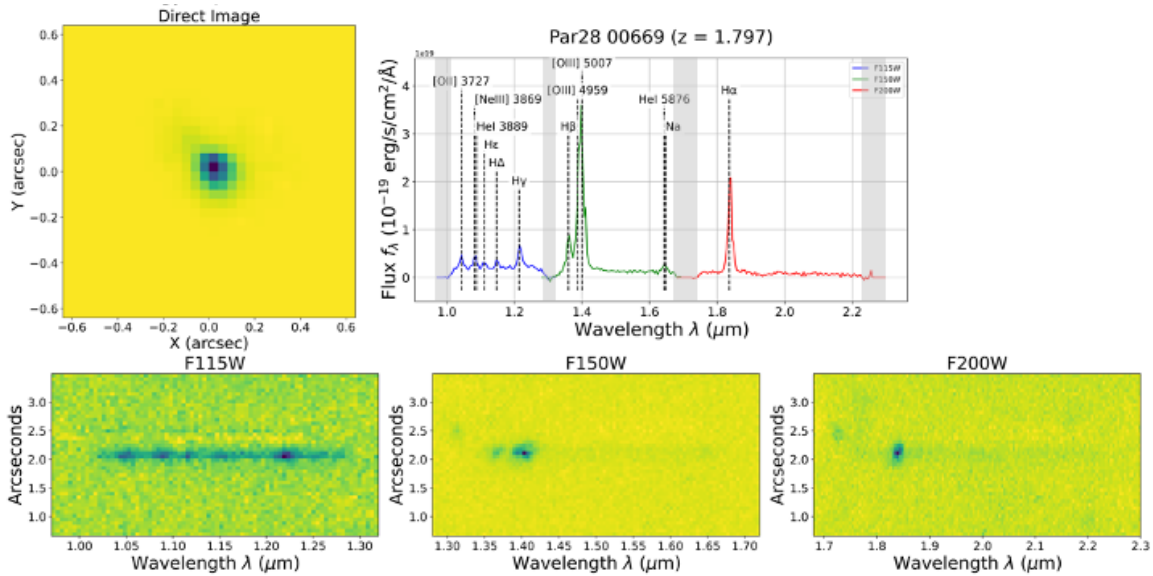


Figure 7. A line-rich EELG from the Par 28 field, shown in the same format as Figure 5. The object exhibits strong [O III], [O II], and Balmer emission from H γ through H α , visible across all three grism filters.

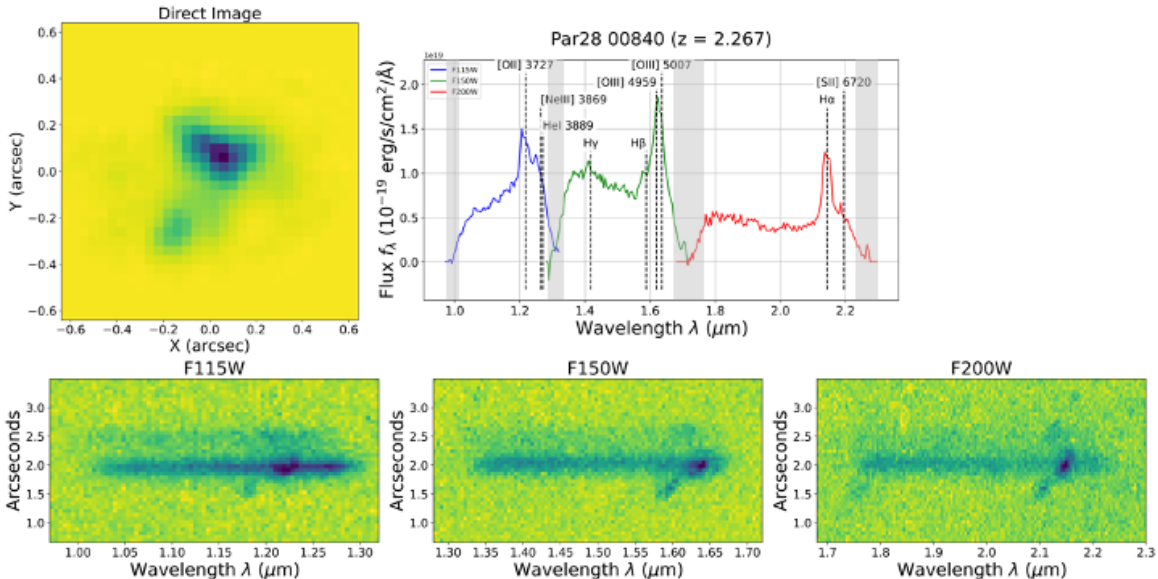


Figure 8. A clumpy or interacting EELG from Par 28, displayed in the same layout as Figure 5. The disturbed morphology and extended emission in the 2D spectrum suggest merging components.

R. C. Kennicutt & N. J. Evans (2012) calibration and are corrected for the small dust attenuation inferred from their Balmer decrements.

Our results in Figure 12 show that, first, at the higher redshifts of many PASSAGE galaxies ($z > 1$), they tend to have higher specific star formation rates, resulting in higher H α equivalent widths. Second, the observed SFMS increases toward lower masses and higher H α equivalent width; therefore PASSAGE is particularly sensitive to very low-mass galaxies that are undergoing intense bursts of star formation.

4.2. Dust Reddening

Dust attenuation traced by the Balmer decrement, H α /H β , has been shown to correlate with various galaxy properties such as stellar mass, gas-phase metallicity, SFR (T. Garn &

P. N. Best 2010; H. J. Zahid et al. 2014; A. J. Battisti et al. 2022; A. E. Shapley et al. 2022), and, more recently, velocity dispersion (G. Maheson et al. 2024). Among these properties, the primary dependence has been found to be on stellar mass (G. Maheson et al. 2024). Recently, A. E. Shapley et al. (2023) used JWST/NIRSpec data from the CEERS program to study the dust attenuation–stellar mass relation at higher redshifts, $z = 3\text{--}6$ (G. Roberts-Borsani et al. 2025). However, the positive correlation between dust attenuation and stellar mass has mostly been studied in galaxies with $M_* > 10^9 M_\odot$. Existing studies of dust attenuation in lower-mass galaxies are primarily based on stacks of low-resolution, low-S/N spectra (e.g., A. Domínguez et al. 2013; A. J. Battisti et al. 2022).

PASSAGE is obtaining hundreds (and ultimately a few thousand) of individual “gold standard” gas extinction

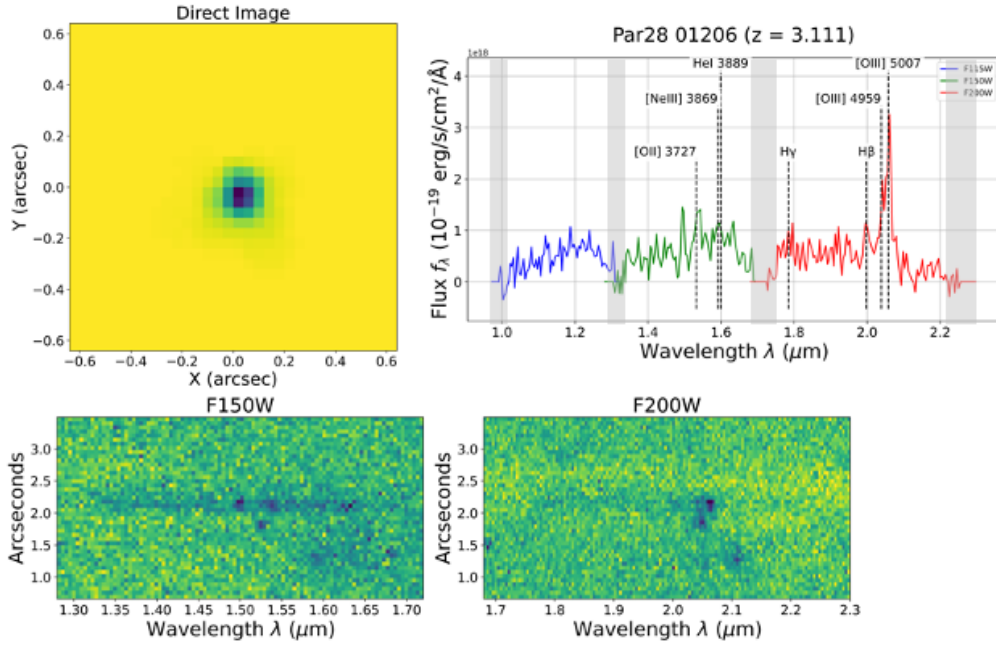


Figure 9. A compact galaxy at $z \approx 3$ from Par 28, shown in the same format as Figure 5. It displays moderate emission from [O II], [O III], and $H\beta$, offering useful spectral diagnostics at intermediate redshift.

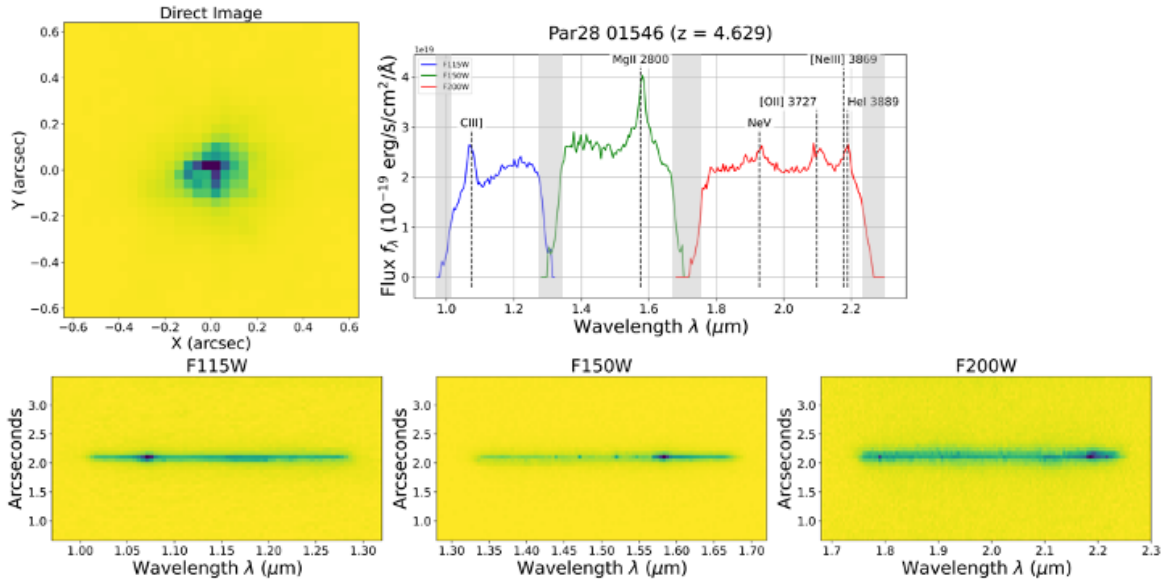


Figure 10. A high-redshift ($z \approx 4.6$) compact galaxy from Par 28, shown in the same format as Figure 5. Strong broad rest-frame UV features including C III] $\lambda 1909$ and Mg II $\lambda 2800$ indicate this is a quasar.

measurements using the $H\alpha/H\beta$ ratio at $1.1 \lesssim z \lesssim 2.4$, down to stellar masses of a few times $10^7 M_\odot$, 10 times less massive than current measurements (A. Domínguez et al. 2013; N. A. Reddy et al. 2015; A. J. Battisti et al. 2022), as seen in Figure 13. To account statistically for blending of [N II] with $H\alpha$, we can rely on established calibrations for the [N II]/ $H\alpha$ ratio as a function of stellar mass and redshift (A. L. Faisst et al. 2018), which are calibrated up to $z \sim 2.5$ and have been used previously for measuring Balmer decrements from low-spectral-resolution grism data (e.g., A. J. Battisti et al. 2022). We note that the [N II] correction is not applied to the PASSAGE measurements in Figure 13 because most galaxies have low stellar masses, where the [N II] contribution is $<10\%$

of $H\alpha$ flux (A. L. Faisst et al. 2018). PASSAGE detects large numbers of extreme emission-line galaxies ($EW[\text{O III}] > 300 \text{ \AA}$). Their starlight continuum is extremely faint, suggesting stellar masses as low as $\log(M_*/M_\odot) \sim 7$ that have been missed by most previous surveys. Figure 13 shows the correlation of gas extinction (from the Balmer decrement) with stellar mass. Most PASSAGE dwarf galaxies have negligible extinction, but a notable minority are substantially dusty. We note that the individual PASSAGE galaxies shown here are selected to have at least a 3σ detection in $H\beta$, which can bias the sample toward lower attenuation. This is evident in the figure, where many galaxies show negligible or zero attenuation. The Balmer line ratios used here are corrected for Balmer

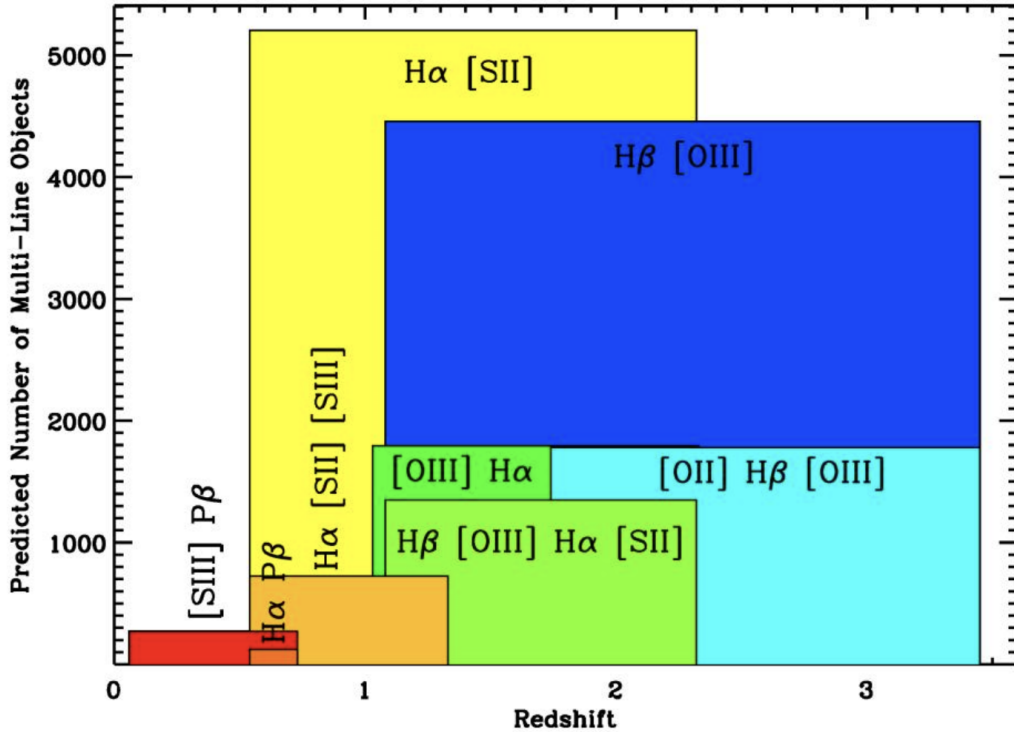


Figure 11. Total predicted multiple emission-line NIRISS galaxies for the 63 fields from PASSAGE, Cycle 1. All lines are detected at 5σ . The height of each box is the expected number of emitters and the width is the span of redshift. Each box is labeled with the set of multiple emission lines it represents. Not all possible line combinations are shown. There will also be many more multiple emission-line sources where only a single line will be detected at 5σ significance, but other lines will be robustly measurable at lower significance. The primary emission lines we use for redshift determinations, $H\alpha$ /[S II] and/or [O III]/ $H\beta$, are predicted to be available in almost 10,000 galaxies. This estimate is confirmed by our detailed inspection of the first PASSAGE fields.

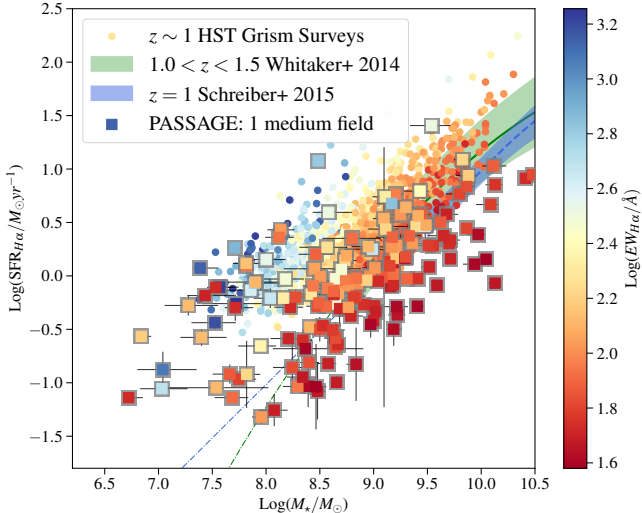


Figure 12. Massive galaxies follow the main sequence SFR– M_* relation (SFMS) at $z \approx 1$, but low-mass galaxies scatter upward to very high $H\alpha$ equivalent widths. Flux incompleteness at low masses ($M_* \sim 10^8 M_\odot$) flattens the slope of the relation. In addition to expanding the low-mass sample size by an order of magnitude, PASSAGE extends the mass regimes down to $10^7 M_\odot$ at $z \sim 2$. The colored squares show detections from a single publicly released NIRISS/WFSS field of medium depth. Stellar masses were estimated from SED fitting, using PASSAGE and COSMOS photometry. SFRs were obtained from $H\alpha$ luminosity, using the R. C. Kennicutt & N. J. Evans (2012) calibration. Error bars show the statistical uncertainties.

absorption lines from the atmosphere of stars, mainly A-type. We used average stellar absorption corrections of 1.4% and 11.8% for $H\alpha$ and $H\beta$, respectively (N. A. Reddy et al. 2015; A. Alavi et al. 2025).

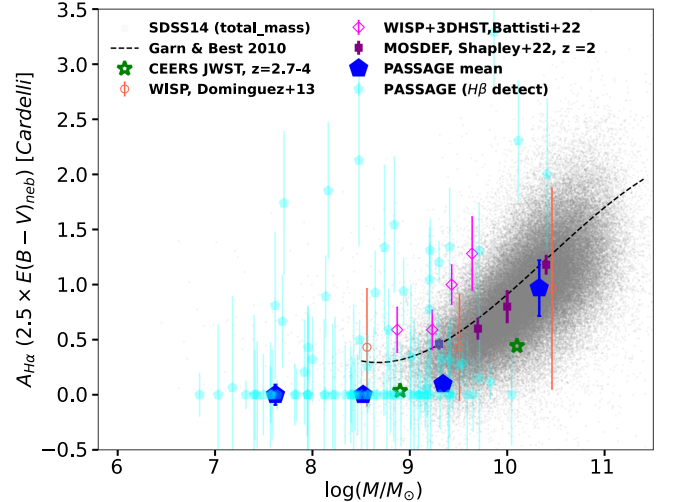


Figure 13. Correlation of gas extinction (i.e., from Balmer decrement) with stellar mass. Error bars show the statistical uncertainties. Most PASSAGE dwarf galaxies have small or negligible extinction, but a significant minority are substantially dusty. On average, our new low-mass galaxies continue the trends found in somewhat more massive galaxies by the WISP survey and substantially more massive galaxies in MOSDEF (A. E. Shapley et al. 2022). Studies such as by A. J. Battisti et al. (2022), B. Lorenz et al. (2024), and A. Domínguez et al. (2013) highlight an offset in the dust attenuation–mass relationship depending on whether the fiber-region stellar mass or the total stellar mass is considered for Sloan Digital Sky Survey (SDSS) galaxies. For the SDSS galaxies, we have used the total stellar mass.

For fields with ancillary photometric data, we can combine the Balmer decrements with SED model fits to this photometry, to derive average dust attenuation curves (N. A. Reddy et al. 2015; A. J. Battisti et al. 2022). Such

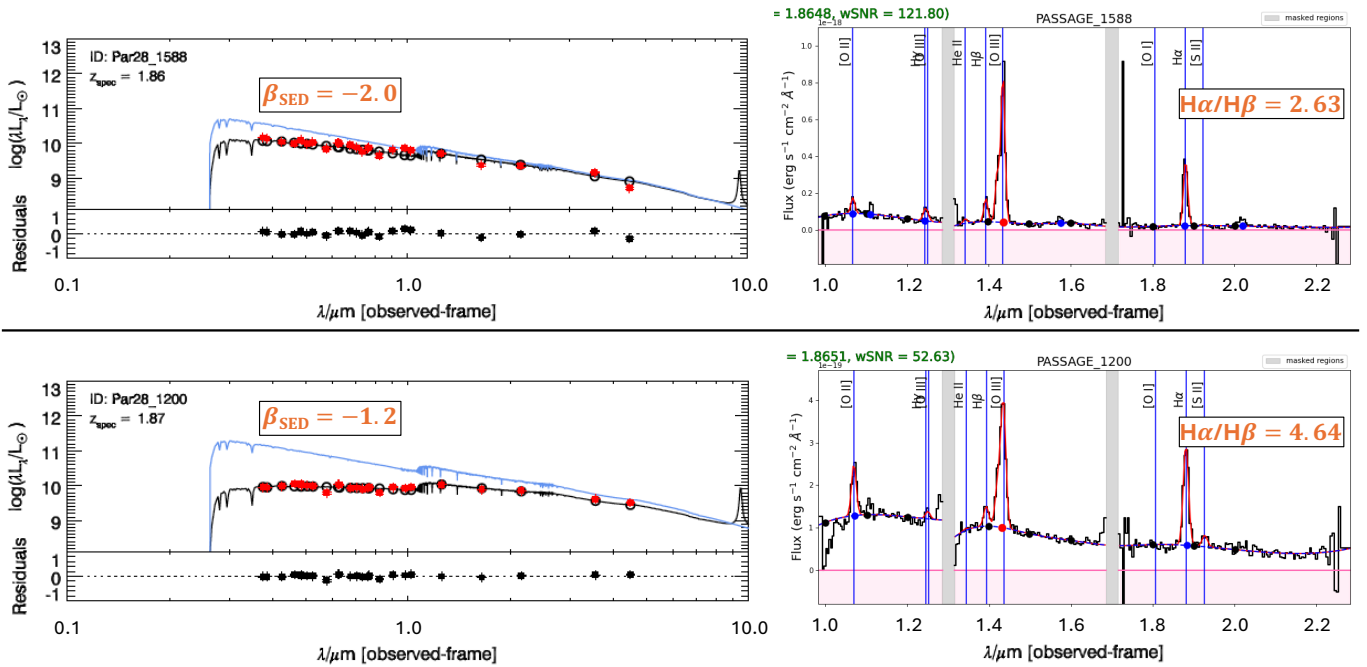


Figure 14. Comparison of the reddening on the stellar continuum UV slope based on an SED fit, $\beta_{\text{SED}} (F_{\lambda} \propto \lambda^{\beta_{\text{SED}}}; 1258 \text{ \AA} \leq \lambda_{\text{rest}} \leq 2580 \text{ \AA}; \text{D. Calzetti et al. 1994})$, relative to the Balmer decrement, $H\alpha/H\beta$, for two galaxies at $z = 1.9$ in the Par 28 field. Left panels show an SED fit (black line) to COSMOS2020 photometry (red symbols; J. R. Weaver et al. 2022) using MAGPHYS (E. da Cunha et al. 2008; A. J. Battisti et al. 2020, mainly to demonstrate the wide rest-frame SED coverage for PASSAGE fields in COSMOS). The blue line is the prediction for the unattenuated stellar continuum. Right panels show the PASSAGE grism spectra. The upper galaxy has a lower Balmer decrement than the lower galaxy, indicating that the lower galaxy is experiencing more dust attenuation. This is reflected in the values of the UV slopes, with the upper left panel having a bluer UV slope than the lower left panel. By comparing SEDs for a large number of galaxies with Balmer decrements, we can derive the average dust attenuation curves and their evolution with galaxy properties.

data are already available for 18 PASSAGE fields (29%) located within the COSMOS footprint, and more will be available in the future from follow-up programs with HST (seven non-COSMOS fields; PI: Mehta, #17461), VLT/FORS2 (nine non-COSMOS fields; PI: Battisti, 114.27EF.001, 115.27WC.001/115.27WC.003), and Keck/LRIS (two non-COSMOS fields with grism data in all three filters; PI: Nedkova, 64/2025A_N067). This is illustrated in Figure 14, which contrasts examples of an emission-line galaxy (top) that has little if any extinction in either its starlight or gas with another galaxy (bottom) that has substantial continuum and emission-line reddenings. We will further constrain the optical shape of the dust extinction curve using higher-order Balmer lines (via stacking; e.g., N. A. Reddy et al. 2020).

At lower redshifts ($z \leq 0.7$), our longest-wavelength spectral coverage includes the Pa β recombination line. We show the ratio of H α to Pa β for individual galaxies in Figure 15. Not surprisingly, no galaxies have observed ratios comparable to the intrinsic ratio predicted by pure Case B recombination (top dotted line). Instead, as expected, many galaxies have significantly weaker H α , which is in most cases consistent with the standard expectation of 1 mag of absorption at H α (R. C. Kennicutt 1983). Interestingly, a significant fraction (four out of eight) of the galaxies have H α even considerably weaker, indicative of 2 mag or more of dust extinction.

4.3. Extreme Emission-line Galaxies

The slitless spectroscopy of PASSAGE is able to detect emission lines independently of the underlying continuum brightness. Thus in contrast to typical magnitude-limited spectral surveys, PASSAGE selects an emission-line flux-

limited sample of galaxies rather than a continuum flux-limited sample. PASSAGE can measure galaxies with emission lines of extremely high equivalent widths even when the continuum is very faint. This results in a large new sample of so-called “extreme emission-line galaxies” (EELGs), which have line equivalent widths exceeding 200 Å to more than 1000 Å (H. Atek et al. 2011, 2014). Such extreme but faint galaxies tend to be excluded from traditional spectroscopic surveys (N. Chen et al. 2024).

Figures 5, 6, 7, 8, and 9 show examples of PASSAGE EELGs. They have H α emission lines with rest-frame equivalent widths of a few hundred angstroms or more, indicative of extremely high specific star formation rates larger than 10^{-8} yr^{-1} . These imply that much of the star formation in these galaxies happened within a hundred million years of the epoch at which we observe them (H. Atek et al. 2014). The low spectral resolution of the NIRISS grism blends in the [N II] $\lambda\lambda 6584/6548$ doublet with H α . However, we can remove the [N II] contamination with a statistical correction, which indicates that it is a small contributor in typical EELGs. The corresponding timescale to double their stellar masses may be only $\sim 10^8 \text{ yr}$ (H. Atek et al. 2014; K. Boyett et al. 2022). Furthermore, their intense bursts of star formation are often concentrated into extremely small volumes (H. Atek et al. 2011). It is not always easy to classify these highly disturbed dynamical systems into individual galaxies or assembling galaxy fragments.

PASSAGE finds as many as 100 such extreme H α emitters per field, out to redshifts of $z \sim 2.5$. For example, Figure 12 shows that for galaxies with $\text{EW}(H\alpha) > 200 \text{ \AA}$, the light blue and dark blue points dominate the PASSAGE sample of spectra in this single field. Figure 12 also illustrates that larger

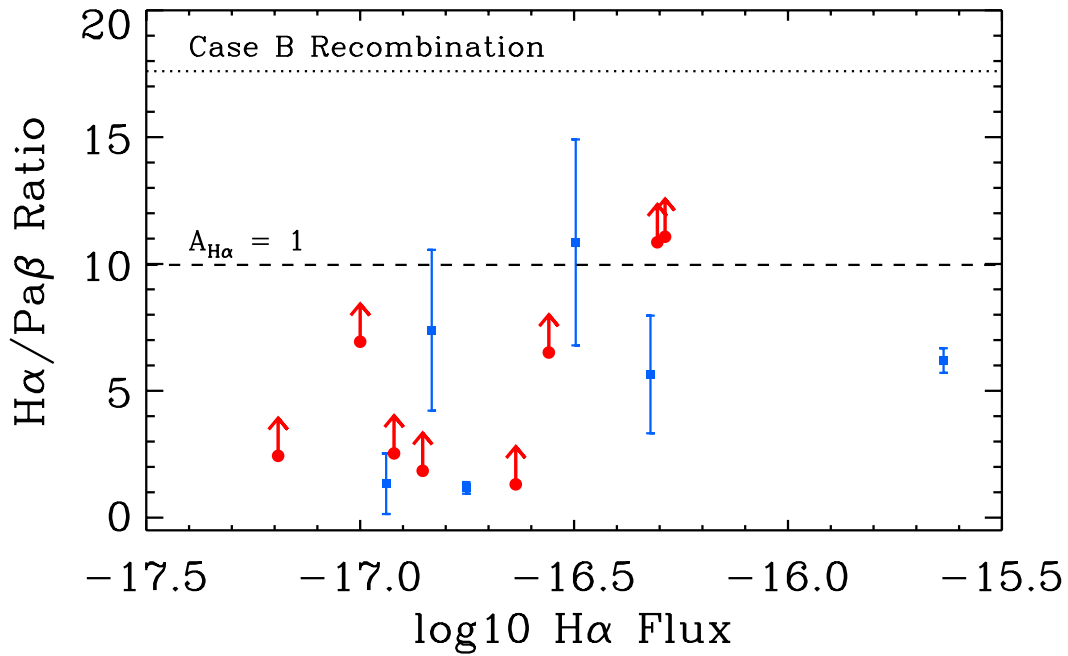


Figure 15. PASSAGE measurements of the reddening-sensitive Balmer to Paschen emission-line ratio in a small sample of galaxies at $z \leq 0.7$. These are plotted as a function of $H\alpha$ line flux in cgs units. The dotted horizontal line shows the predicted intrinsic ratio of $H\alpha/Pa\beta$ for Case B recombination with no extinction, $A_{H\alpha} = 0$. Some detections and upper limits are consistent with the $H\alpha$ to $Pa\beta$ ratio of 10, which is expected based on the typically assumed one magnitude of extinction at the wavelength of $H\alpha$ (shown by the dashed line). However, several galaxies show significantly weaker $H\alpha$, indicative of greater reddening.

numbers of EELGs can be inferred from the detection in PASSAGE spectra of [O III] line emission of very high equivalent width out to $z \sim 3.5$. And as illustrated by the example spectra in Figure 10, the strong UV rest-frame emission lines of quasars can be seen in PASSAGE at higher redshifts, out to $z > 5$.

4.4. Gas-phase Mass–Metallicity Relations

The mass–metallicity relation (MZR) is the correlation between galaxies’ stellar masses and their gas-phase metallicities. Constraining this relation over large ranges of stellar mass, and its evolution with redshift, provides crucial constraints on models of gas accretion, star formation, metal enrichment, and outflows, which are responsible for regulating galaxy growth. PASSAGE includes many low-mass galaxies, reaching largely unobserved ranges of stellar mass, gas fraction, and redshift (Figure 16, R. L. Sanders et al. 2018, 2021; A. Henry et al. 2021; X. Wang et al. 2022; M. Curti et al. 2023; M. Revalski et al. 2024). At low stellar masses and high redshifts, outflows may preferentially remove metals (A. Henry et al. 2013), thus making the low-mass MZR slope a key diagnostic of the role of gas recycling at different epochs, and quantifying the role of feedback and of the stochastic processes in regulating metallicity. PASSAGE, due to its large sample size, is also measuring the scatter in the MZR for low-mass galaxies (see, e.g., P. Torrey et al. 2019).

Prior to JWST, these regimes had not been constrained because of the low number and quality of spectra below $10^9 M_{\odot}$, which required stacking. More recent results with NIRISS (M. Li et al. 2023; X. He et al. 2024) have shown the feasibility of metallicity measurements at lower masses, albeit with uncertain values and scatter. PASSAGE addresses this by measuring gas metallicities of many individual low-mass galaxies—without requiring stacking—up to $z = 3.5$.

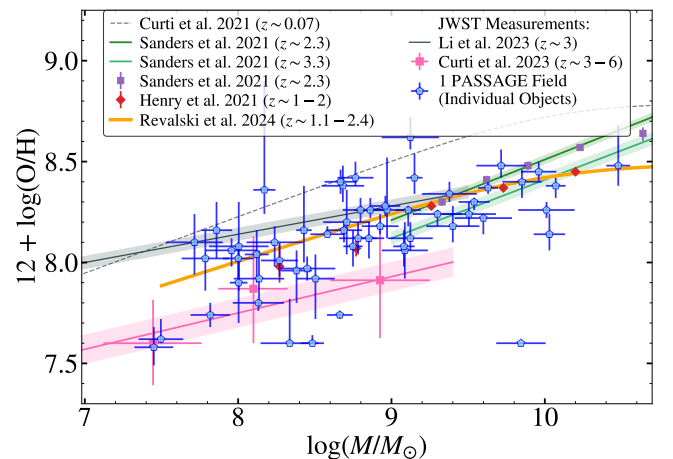


Figure 16. Gas-phase mass–metallicity relation of individual galaxies from one PASSAGE field compared to stacked results from the literature (M. Curti et al. 2017, 2023; A. Henry et al. 2021; R. L. Sanders et al. 2021; M. Li et al. 2023). A single PASSAGE field already extends the relation to objects of low stellar mass at $1.7 \lesssim z \lesssim 3.4$.

For the several thousand galaxies in the redshift range $1.7 \lesssim z \lesssim 3.5$ for which the multiwavelength coverage of the PASSAGE grism filters allows simultaneous detection of [O II], [O III], and $H\beta$ lines, we are able to determine the MZR using strong-line diagnostics such as the R_{23} index (e.g., B. E. J. Pagel et al. 1979; C. A. Tremonti et al. 2004). In Figure 16, we show the position of 58 individual galaxies from a single deep PASSAGE field on the stellar mass–metallicity plane. These objects are selected to have $S/N \geq 10$ [O III] detections. Metallicities are obtained using the M. Curti et al. (2017) strong-line calibrations, which have been validated out to at least $z \sim 2.5$ (M. Revalski et al. 2024), and their stellar masses are derived as described in Section 4.1.

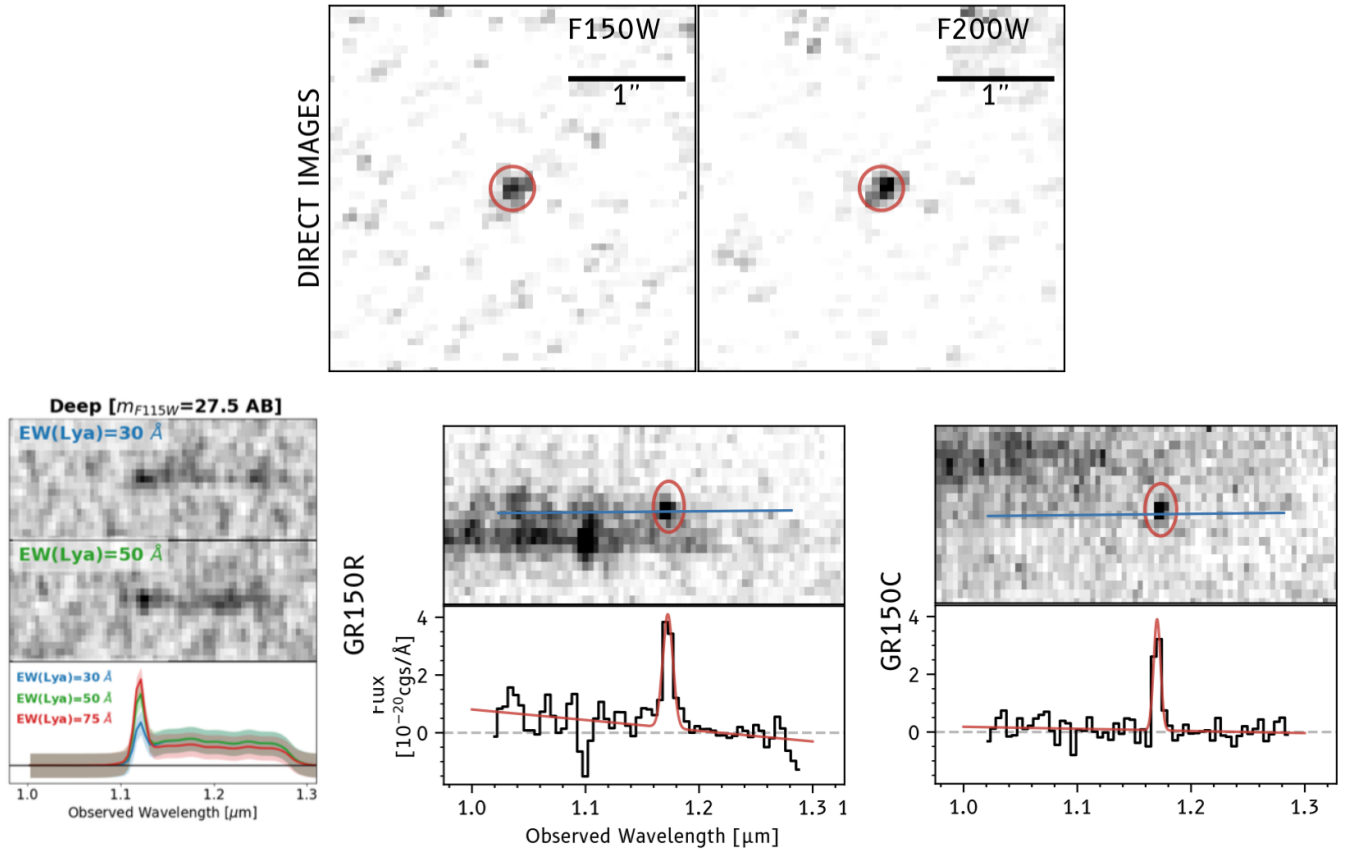


Figure 17. PASSAGE is able to measure Ly α emission (LAE) with rest-frame EW $> 50 \text{ \AA}$ in spectroscopically confirmed $z > 8$ galaxies. The lower left panel shows simulated $z = 8.2$ LAE spectra with $m_{F115W} = 27.5$ (deep) with rest-frame EW(Ly α) of 30 \AA (top row) and 50 \AA (middle row). These are predicted to have clear Ly α detections. The bottom subpanel shows the simulated 1D spectra along with their noise for a range of EWs. These simulations are then compared with an actual PASSAGE detection of Ly α line emission. The lower right panels show the 2D and 1D F115W spectra for the object (visible in the direct images above), for both grism orientations, with the original spectral wavelength scales running along rows, and then along columns. Although these different orientations result in different nearby spectra, in both cases the Ly α line is independently detected at the same location and wavelength. The observed 2D spectrograms are $1''/4$ high, while the simulated spectral images to the left are on approximately the same scale.

Due to the long-lasting interplay between the processes that drive the baryon cycle, the metallicity of galaxies has also been observed to anticorrelate with star formation rate at fixed stellar mass. This relation is commonly referred to as the “fundamental metallicity relation” (FMR; e.g., S. L. Ellison et al. 2008; F. Mannucci et al. 2010; S. Salim et al. 2015; O. G. Telford et al. 2016; W. M. Baker et al. 2023). PASSAGE is now establishing whether high-redshift galaxies follow the FMR as at $z \sim 0$ (F. Mannucci et al. 2010).

In addition to integrated metallicities, PASSAGE has measured spatially resolved metallicity, and the consequent mass-metallicity gradient relation (MZGR) at $z \sim 2$ –3 (A. Acharyya et al. 2025).

4.5. Absorption-line Measurements

Stellar age and abundance measurements from absorption-line spectroscopy generally require rest-frame coverage from 3700 to 5300 \AA . PASSAGE obtains this at $1.6 < z < 2$ for all medium and long visits, and at $2.0 < z < 3.3$ for long visits that include the F200W spectral band. In each field we typically find around a few spectra of $z = 1.6$ – 2.5 quiescent galaxies that are bright enough ($m_{F115W} \lesssim 24.5$) to have very high S/N $_{F115W}$ (10 or larger) per spectral pixel. In these cases, although emission lines are either weak or undetected, we can

measure diagnostic stellar absorption features. If we restrict consideration to the strongest stellar absorptions—the Balmer and Ca II HK breaks—these can be measured even when the continuum is one to two magnitudes fainter, giving us an average of ~ 5 such spectra per field.

4.6. Feasibility of Spectroscopically Identifying and Measuring Ly α lines in High-redshift Galaxies

The total F115W grism exposures that are useful to search for faint Ly α lines and breaks in the Ly α forest at $z \geq 8$ range from 8 ks to more than 20 ks in the deepest parallel visits. In the simulation shown in the lower left panel of Figure 17, a Ly α emission line is added to the spectrum of a Lyman break galaxy (LBG). Even for these faint galaxies, the continuum break and the line are confidently detected, for rest-frame line equivalent widths as small as 50 \AA .

We have made a careful search of our deepest PASSAGE fields for strong isolated emission lines in the 1.0–1.3 μm range. This special “by-hand” analysis does not require that any object be initially detected in the broadband images. It has revealed four new Ly α emission lines at redshifts of $z = 7.7$ – 9.5 (A. Runnholm et al. 2025). Their equivalent widths range from 40 to 100 \AA .

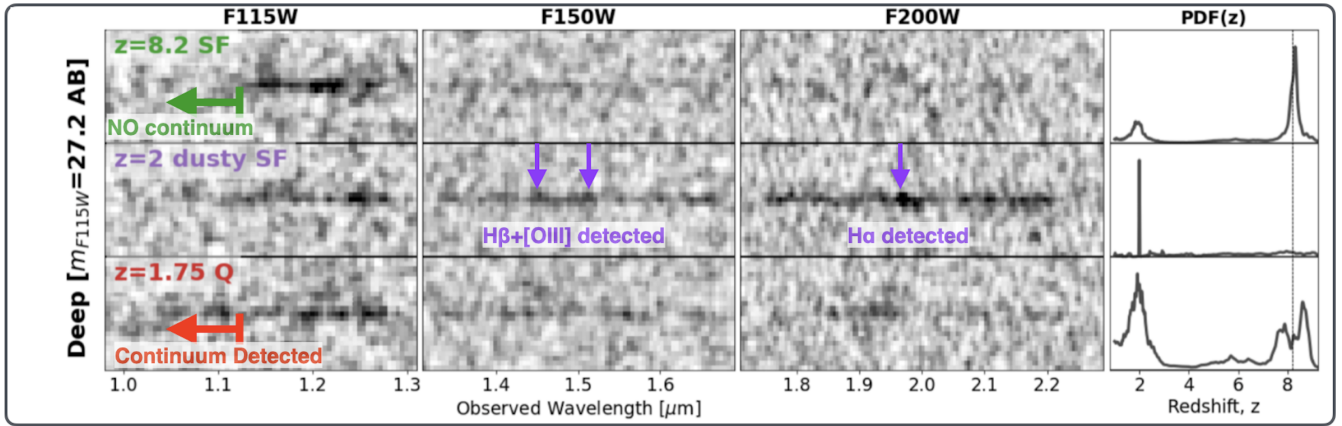


Figure 18. PASSAGE can distinguish between $z > 8$ Lyman break galaxies and low-redshift contaminants. A simulated $z = 8.2$ LBG is shown in the top row, detected by its Ly α break (rest-frame 1216 Å) in the deep observations. The slitless 2D spectra for the F115W, F150W, and F200W filters run from left to right. The spatial (vertical) scale is the same as in Figure 17. The last column shows the redshift probability distribution from template fitting. This simulation shows that PASSAGE correctly distinguishes between a $z \sim 8$ LBG and a $z = 2$ dusty star-forming galaxy (middle row) or a $z = 1.75$ passive galaxy (bottom row), which are prime contaminants. We caution that if not all three wavelength regions are available, and no emission lines are detected, then the probability density functions (PDFs) for the high- and low-redshift solutions are not so unambiguously distinguished.

Figure 18 shows a simulated grism spectrum for a Lyman break galaxy emitting stellar continuum only. Although there is no Ly α emission line in the simulation, since there are many observed continuum pixels above and below the Lyman break (at $1.12 \mu\text{m} = 1216 \text{Å} \times 9.2$), this sharp break is detected. And, it is distinguishable from the gradual downturns seen in $z = 2$ interloper galaxies, even if they lack any rest-frame optical emission lines. NIRISS slitless spectra have indeed detected Lyman breaks in two out of three faint $z \sim 8$ galaxies (G. Roberts-Borsani et al. 2022), with magnitudes and integration times similar to these simulations.

5. Summary and Legacy Impact of PASSAGE

Synergies with other programs and missions. The JWST/NIRISS capability for slitless near-infrared spectroscopy in a large number of parallel fields has opened many new prospects for better understanding galaxy evolution. Our preliminary analysis of the first PASSAGE observations demonstrates that the performance of this mode is as good as, or even better than, was anticipated before launch. We show recent NIRISS examples of major improvements in sensitivity and extended long-wavelength coverage, to allow advances in the study of galaxies at higher redshifts and lower stellar masses than were previously attainable. We highlight progress in studying the star formation main sequence, the mass/metallicity correlation, and gas reddening. PASSAGE complements ongoing deep JWST spectroscopy of selected fields and targets, by measuring galaxy spectra without preselection in 63 independent fields, to overcome uncertainties due to cosmic variance.

The pure-parallel observations provide a public treasure trove of spectroscopy. This multiplies their future value, allowing for JWST follow-up, as well as complementary data for the Euclid and Roman missions on how to optimize observing strategies. PASSAGE complements those missions by going much deeper in smaller areas of sky, thus conducting science that neither Euclid nor Roman can achieve.

The brighter (and rarer) objects discovered are particularly compelling for follow-up by JWST and other facilities. For example, PASSAGE is discovering galaxies bright enough to measure the key [O III] $\lambda 4363$ line, to test or improve the

calibration of current metallicities at $z \geq 2$ (T. Gburek et al. 2019; R. L. Sanders et al. 2020). Even if the high-redshift strong-line metallicity calibration does need to be revised, this project has provided the essential suite of lines on which it is based.

Legacy value of public fully processed data sets in the archive. High-level science products (HLSPs) are used up to 10 times more than individual calibrated data, and the archive of slitless spectroscopy is sure to provide an unprecedented legacy of lasting scientific value. We will deliver fully processed data and HLSPs to MAST for the astronomy community.

Acknowledgments


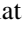
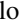

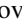

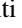
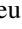
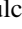
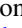

We acknowledge support by NASA through grant JWST-GO-1571 (PI: Malkan). We are very grateful to staff members at Space Telescope Science Institute, who worked hard to schedule pure-parallel opportunities for this project, especially to our Program Coordinator Shelly Meyett. We thank the anonymous referee, for making extremely thorough readings and providing many suggestions that have improved this paper. The JWST data presented in this article were obtained from the Mikulski Archive for Space Telescopes (MAST) at the Space Telescope Science Institute. The specific observations analyzed can be accessed via doi:[10.17909/6ca5-ba17](https://doi.org/10.17909/6ca5-ba17).

X.W. is supported by the National Natural Science Foundation of China (grant 12373009), the CAS Project for Young Scientists in Basic Research grant No. YSBR-062, the Fundamental Research Funds for the Central Universities, the Xiaomi Young Talents Program, and the science research grant from the China Manned Space Project. B.V., A.A., and P.W. acknowledge support from the INAF Large Grant 2022 “Extragalactic Surveys with JWST” (PI Pentericci) and from the European Union—NextGenerationEU RFF M4C2 1.1 PRIN 2022 project 2022ZSL4BL INSIGHT. P.W. and B.V. acknowledge support from the INAF Mini Grant “1.05.24.07.01 RSN 1: Spatially Resolved Near-IR Emission of Intermediate-Redshift Jellyfish Galaxies” (PI Watson). A.J.B. acknowledges funding from the “FirstGalaxies” Advanced Grant from the European Research Council (ERC) under the European Union’s Horizon

2020 research and innovation program (grant agreement No. 789056). H.A. is supported by CNES, focused on the JWST mission and the Programme National Cosmology and Galaxies (PNCG) of CNRS/INSU with INP and IN2P3, cofunded by CEA and CNES. M.B. acknowledges support from the ERC Grant FIRSTLIGHT and from the Slovenian national research agency ARRS through grants N1-0238 and P1-0188. M.J.H. is fellow of the Knut & Alice Wallenberg Foundation. Y.D. acknowledges the support of the National Key R&D Program of China under grant No. 2022YFA1605300 and the National Nature Science Foundation of China (NSFC) grant No.12273051.

ORCID iDs

Matthew A. Malkan  <https://orcid.org/0000-0001-6919-1237>
 Vihang Mehta  <https://orcid.org/0000-0001-7166-6035>
 Ayan Acharyya  <https://orcid.org/0000-0003-4804-7142>
 Hollis B. Akins  <https://orcid.org/0000-0003-3596-8794>
 Anahita Alavi  <https://orcid.org/0000-0002-8630-6435>
 Hakim Atek  <https://orcid.org/0000-0002-7570-0824>
 Ivano Baronchelli  <https://orcid.org/0000-0003-0556-2929>
 Andrew J. Battisti  <https://orcid.org/0000-0003-4569-2285>
 Kit Boyett  <https://orcid.org/0000-0003-4109-304X>
 Marusa Bradac  <https://orcid.org/0000-0001-5984-0395>
 Sean Tyler Bruton  <https://orcid.org/0000-0002-6503-5218>
 Andrew J. Bunker  <https://orcid.org/0000-0002-8651-9879>
 Adam J. Burgasser  <https://orcid.org/0000-0002-6523-9536>
 Caitlin M. Casey  <https://orcid.org/0000-0002-0930-6466>
 Nuo Chen  <https://orcid.org/0000-0002-0486-5242>
 James Colbert  <https://orcid.org/0000-0001-6482-3020>
 Y. Sophia Dai  <https://orcid.org/0000-0002-7928-416X>
 Maximilien Franco  <https://orcid.org/0000-0002-3560-8599>
 Clea Hannahs  <https://orcid.org/0009-0009-0868-8165>
 Santosh Harish  <https://orcid.org/0000-0003-0129-2079>
 Farhanul Hasan  <https://orcid.org/0000-0002-0072-0281>
 Matthew J. Hayes  <https://orcid.org/0000-0001-8587-218X>
 Alaina L. Henry  <https://orcid.org/0000-0002-6586-4446>
 Mason Huberty  <https://orcid.org/0009-0002-9932-4461>
 Tucker Jones  <https://orcid.org/0000-0001-5860-3419>
 Jeyhan S. Kartaltepe  <https://orcid.org/0000-0001-9187-3605>
 Keunho J. Kim  <https://orcid.org/0000-0001-6505-0293>
 Nicha Leethochawalit  <https://orcid.org/0000-0003-4570-3159>
 Jacob Levine  <https://orcid.org/0009-0000-9478-1933>
 Sijia Li  <https://orcid.org/0000-0003-4813-8482>
 Yu-Heng Lin  <https://orcid.org/0000-0001-8792-3091>
 Yixiao Liu  <https://orcid.org/0009-0006-4990-7529>
 Charlotte Mason  <https://orcid.org/0000-0002-3407-1785>
 Daniel Masters  <https://orcid.org/0000-0001-5382-6138>
 Henry Joy McCracken  <https://orcid.org/0000-0002-9489-7765>
 Takahiro Morishita  <https://orcid.org/0000-0002-8512-1404>
 Kalina V. Nedkova  <https://orcid.org/0000-0001-5294-8002>
 Marc Rafelski  <https://orcid.org/0000-0002-9946-4731>
 Guido Roberts-Borsani  <https://orcid.org/0000-0002-4140-1367>
 Axel Runnholm  <https://orcid.org/0000-0002-1025-7569>
 Michael J. Rutkowski  <https://orcid.org/0000-0001-7016-5220>
 Alberto Saldana-Lopez  <https://orcid.org/0000-0001-8419-3062>

Zahra Sattari  <https://orcid.org/0000-0002-0364-1159>
 Claudia Scarlata  <https://orcid.org/0000-0002-9136-8876>
 Kasper Borello Schmidt  <https://orcid.org/0000-0002-3418-7251>
 Marko Shuntov  <https://orcid.org/0000-0002-7087-0701>
 Harry Teplitz  <https://orcid.org/0000-0002-7064-5424>
 Michele Trenti  <https://orcid.org/0000-0001-9391-305X>
 Tommaso Treu  <https://orcid.org/0000-0002-8460-0390>
 Benedetta Vulcani  <https://orcid.org/0000-0003-0980-1499>
 Peter J. Watson  <https://orcid.org/0000-0003-3108-0624>
 Xin Wang  <https://orcid.org/0000-0002-9373-3865>
 Zhuyun Zhuang  <https://orcid.org/0000-0002-1945-2299>

References

- Acharyya, A., Watson, P. J., Vulcani, B., et al. 2025, arXiv:2508.05335
 Alavi, A., Siana, B., Richard, J., et al. 2016, *ApJ*, 832, 56
 Alavi, A., Siana, B., Teplitz, H. I., et al. 2025, arXiv:2510.00427
 Amorín, R., Fontana, A., Pérez-Montero, E., et al. 2017, *NatAs*, 1, 0052
 Atek, H., Kneib, J.-P., Pacífici, C., et al. 2014, *ApJ*, 789, 96
 Atek, H., Malkan, M., McCarthy, P., et al. 2010, *ApJ*, 723, 104
 Atek, H., Siana, B., Scarlata, C., et al. 2011, *ApJ*, 743, 121
 Backhaus, B. E., Trump, J. R., Pirzkal, N., et al. 2024, *ApJ*, 962, 195
 Bagley, M. B., Scarlata, C., Henry, A., et al. 2017, *ApJ*, 837, 11
 Bagley, M. B., Scarlata, C., Mehta, V., et al. 2020, *ApJ*, 897, 98
 Baker, W. M., Maiolino, R., Belfiore, F., et al. 2023, *MNRAS*, 519, 1149
 Barbary, K. 2016, *JOSS*, 1, 58
 Battisti, A. J., Bagley, M. B., Baronchelli, I., et al. 2022, *MNRAS*, 513, 4431
 Battisti, A. J., Bagley, M. B., Rafelski, M., et al. 2024, *MNRAS*, 530, 894
 Battisti, A. J., da Cunha, E., Shivaeei, I., & Calzetti, D. 2020, *ApJ*, 888, 108
 Becker, G. D., Davies, F. B., Furlanetto, S. R., et al. 2018, *ApJ*, 863, 92
 Bertin, E., & Arnouts, S. 1996, *A&AS*, 117, 393
 Boyett, K., Bunker, A. J., Curtis-Lake, E., et al. 2024, *MNRAS*, 535, 1796
 Boyett, K., Mascia, S., Pentericci, L., et al. 2022, *ApJL*, 940, L52
 Bradač, M., Strait, V., Mowla, L., et al. 2024, *ApJL*, 961, L21
 Brammer, G. 2023, grizli, Version 1.9.11, Zenodo, doi:10.5281/zenodo.1146904
 Bunker, A. J., Warren, S. J., Hewett, P. C., & Clements, D. L. 1995, *MNRAS*, 273, 513
 Calzetti, D., Kinney, A. L., & Storchi-Bergmann, T. 1994, *ApJ*, 429, 582
 Cardelli, J. A., Clayton, G. C., & Mathis, J. S. 1989, *ApJ*, 345, 245
 Carnall, A. C., McLure, R. J., Dunlop, J. S., & Davé, R. 2018, *MNRAS*, 480, 4379
 Casey, C. M., Kartaltepe, J. S., Drakos, N. E., et al. 2023, *ApJ*, 954, 31
 Chen, N., Motohara, K., Spitler, L., et al. 2024, *ApJ*, 964, 5
 Colbert, J., Mehta, V., Alavi, A., et al. 2024, AAS Meeting, 56, 325.02
 Curti, M., Cresci, G., Mannucci, F., et al. 2017, *MNRAS*, 465, 1384
 Curti, M., D'Eugenio, F., Carniani, S., et al. 2023, *MNRAS*, 518, 425
 da Cunha, E., Charlot, S., & Elbaz, D. 2008, *MNRAS*, 388, 1595
 Davé, R., Anglés-Alcázar, D., Narayanan, D., et al. 2019, *MNRAS*, 486, 2827
 Davé, R., Rafieferantsoa, M. H., Thompson, R. J., & Hopkins, P. F. 2017, *MNRAS*, 467, 115
 Davies, J. 2024, snowblind, 0.2.1, <https://github.com/mpi-astronomy/snowblind>
 De Rossi, M. E., Bower, R. G., Font, A. S., Schaye, J., & Theuns, T. 2017, *MNRAS*, 472, 3354
 Dey, A., Schlegel, D. J., Lang, D., et al. 2019, *AJ*, 157, 168
 Domínguez, A., Siana, B., Brooks, A. M., et al. 2015, *MNRAS*, 451, 839
 Domínguez, A., Siana, B., Henry, A. L., et al. 2013, *ApJ*, 763, 145
 Doyon, R., Willott, C. J., Hutchings, J. B., et al. 2023, *PASP*, 135, 098001
 Ellison, S. L., Patton, D. R., Simard, L., & McConnachie, A. W. 2008, *ApJL*, 672, L107
 Estrada-Carpenter, V., Sawicki, M., Brammer, G., et al. 2024, *MNRAS*, 532, 577
 Euclid Collaboration, Gabarra, L., Mancini, C., et al. 2023, *A&A*, 676, A34
 Faísst, A. L., Masters, D., Wang, Y., et al. 2018, *ApJ*, 855, 132
 Garn, T., & Best, P. N. 2010, *MNRAS*, 409, 421
 Gburek, T., Siana, B., Alavi, A., et al. 2019, *ApJ*, 887, 168
 Gordon, K. D., Clayton, G. C., Misselt, K. A., Landolt, A. U., & Wolff, M. J. 2003, *ApJ*, 594, 279
 Grogin, N. A., Kocevski, D. D., Faber, S. M., et al. 2011, *ApJS*, 197, 35
 He, X., Wang, X., Jones, T., et al. 2024, *ApJL*, 960, L13
 Henry, A., Rafelski, M., Sunquist, B., et al. 2021, *ApJ*, 919, 143

- Henry, A., Scarlata, C., Domínguez, A., et al. 2013, *ApJL*, **776**, L27
- Hicks, E. K. S., Malkan, M. A., Teplitz, H. I., McCarthy, P. J., & Yan, L. 2002, *ApJ*, **581**, 205
- Kashikawa, N., Shimasaku, K., Malkan, M. A., et al. 2006, *ApJ*, **648**, 7
- Kashikawa, N., Shimasaku, K., Matsuda, Y., et al. 2011, *ApJ*, **734**, 119
- Kennicutt, R. C., Jr 1983, *ApJ*, **272**, 54
- Kennicutt, R. C., Jr 1998, *ARA&A*, **36**, 189
- Kennicutt, R. C., Jr, & Evans, N. J., II 2012, *ARA&A*, **50**, 531
- Koekemoer, A. M., Aussel, H., Calzetti, D., et al. 2007, *ApJS*, **172**, 196
- Koekemoer, A. M., Faber, S. M., Ferguson, H. C., et al. 2011, *ApJS*, **197**, 36
- Leja, J., Carnall, A. C., Johnson, B. D., Conroy, C., & Speagle, J. S. 2019, *ApJ*, **876**, 3
- Li, M., Cai, Z., Bian, F., et al. 2023, *ApJL*, **955**, L18
- Lilly, S. J., Carollo, C. M., Pipino, A., Renzini, A., & Peng, Y. 2013, *ApJ*, **772**, 119
- Lorenz, B., Kriek, M., Shapley, A. E., et al. 2024, *ApJ*, **975**, 187
- Ly, C., Malkan, M. A., Kashikawa, N., et al. 2007, *ApJ*, **657**, 738
- Ly, C., Malkan, M. A., Kashikawa, N., et al. 2012, *ApJ*, **757**, 63
- Ly, C., Malkan, M. A., Treu, T., et al. 2009, *ApJ*, **697**, 1410
- Ma, X., Hopkins, P. F., Faucher-Giguère, C.-A., et al. 2016, *MNRAS*, **456**, 2140
- Madau, P., & Dickinson, M. 2014, *ARA&A*, **52**, 415
- Maheson, G., Maiolino, R., Curti, M., et al. 2024, *MNRAS*, **527**, 8213
- Maiolino, R., & Mannucci, F. 2019, *A&ARv*, **27**, 3
- Malkan, M. & WISP Team 2013, in ASP Conf. Ser. 477, *Galaxy Mergers in an Evolving Universe*, ed. W. H. Sun et al. (San Francisco, CA: ASP), 255
- Mannucci, F., Cresci, G., Maiolino, R., Marconi, A., & Gnerucci, A. 2010, *MNRAS*, **408**, 2115
- McCarthy, P. J., Yan, L., Freudling, W., et al. 1999, *ApJ*, **520**, 548
- McCracken, H. J., Milvang-Jensen, B., Dunlop, J., et al. 2012, *A&A*, **544**, A156
- Nedkova, K. V., Häußler, B., Marchesini, D., et al. 2021, *MNRAS*, **506**, 928
- Noeske, K. G., Weiner, B. J., Faber, S. M., et al. 2007, *ApJL*, **660**, L43
- Pagel, B. E. J., Edmunds, M. G., Blackwell, D. E., Chun, M. S., & Smith, G. 1979, *MNRAS*, **189**, 95
- Pirzkal, N., Rothberg, B., Papovich, C., et al. 2024, *ApJ*, **969**, 90
- Ravindranath, S. & Niriss Team 2023, NIRISS Commissioning Results: NIS-015—NIRISS GR150C R Flux Calibration (NGAS CAR-699, APT 1089), Technical Rep. JWST-STScI-008328, STScI
- Reddy, N. A., Kriek, M., Shapley, A. E., et al. 2015, *ApJ*, **806**, 259
- Reddy, N. A., Shapley, A. E., Kriek, M., et al. 2020, *ApJL*, **902**, 123
- Revalski, M., Rafelski, M., Henry, A., et al. 2024, *ApJ*, **966**, 228
- Rihtaršič, G., Bradač, M., Desprez, G., et al. 2025, *A&A*, **696**, A15
- Roberts-Borsani, G., Bagley, M., Rojas-Ruiz, S., et al. 2025, *ApJ*, **983**, 18
- Roberts-Borsani, G., Morishita, T., Treu, T., et al. 2022, *ApJL*, **938**, L13
- Runnholm, A., Hayes, M. J., Mehta, V., et al. 2025, *ApJ*, **984**, 95
- Saintonge, A., Kauffmann, G., Wang, J., et al. 2011, *MNRAS*, **415**, 61
- Salim, S., Lee, J. C., Davé, R., & Dickinson, M. 2015, *ApJ*, **808**, 25
- Sanders, R. L., Jones, T., Shapley, A. E., et al. 2020, *ApJL*, **888**, L11
- Sanders, R. L., Shapley, A. E., Jones, T., et al. 2021, *ApJ*, **914**, 19
- Sanders, R. L., Shapley, A. E., Kriek, M., et al. 2018, *ApJ*, **858**, 99
- Scoville, N., Aussel, H., Brusa, M., et al. 2007, *ApJS*, **172**, 1
- Shapley, A. E., Sanders, R. L., Reddy, N. A., Topping, M. W., & Brammer, G. B. 2023, *ApJ*, **954**, 157
- Shapley, A. E., Sanders, R. L., Salim, S., et al. 2022, *ApJ*, **926**, 145
- Shen, S., Madau, P., Conroy, C., Governato, F., & Mayer, L. 2014, *ApJ*, **792**, 99
- Sparre, M., Hayward, C. C., Feldmann, R., et al. 2017, *MNRAS*, **466**, 88
- Tacconi, L. J., Genzel, R., & Sternberg, A. 2020, *ARA&A*, **58**, 157
- Telford, O. G., Dalcanton, J. J., Skillman, E. D., & Conroy, C. 2016, *ApJ*, **827**, 35
- Teplitz, H. I., Malkan, M. A., & McLean, I. S. 1999, *ApJ*, **514**, 33
- Torrey, P., Vogelsberger, M., Hernquist, L., et al. 2018, *MNRAS*, **477**, L16
- Torrey, P., Vogelsberger, M., Marinacci, F., et al. 2019, *MNRAS*, **484**, 5587
- Tremonti, C. A., Heckman, T. M., Kauffmann, G., et al. 2004, *ApJ*, **613**, 898
- Treu, T., Schmidt, K. B., Brammer, G. B., et al. 2015, *ApJ*, **812**, 114
- van der Wel, A., Franx, M., van Dokkum, P. G., et al. 2014, *ApJ*, **788**, 28
- Wang, X., Li, Z., Cai, Z., et al. 2022, *ApJ*, **926**, 70
- Watson, P. J., Vulcani, B., Treu, T., et al. 2025, *A&A*, **699**, A225
- Weaver, J. R., Kauffmann, O. B., Ilbert, O., et al. 2022, *ApJS*, **258**, 11
- Willott, C. J., Doyon, R., Albert, L., et al. 2022, *PASP*, **134**, 025002
- Yan, L., McCarthy, P. J., Freudling, W., et al. 1999, *ApJL*, **519**, L47
- Zahid, H. J., Dima, G. I., Kudritzki, R.-P., et al. 2014, *ApJ*, **791**, 130